Solver Guide for the MATLAB pulse propagation in bulk solid or gas

Yi-Hao Chen

Applied and Engineering Physics, Cornell University

June 17, 2025

Contents

CONTENTS

Cornell University

Chapter 1

Overview

1.1 High-level understanding of this package

This package is designed to solve for nonlinear pulse propagation in bulk space (*e.g.*, crystals, gases, or free space). It's originally designed to solve for multimode fibers, but it can also be used for general bulk medium with a customized index profile. Therefore, it can simulation multipass cells and multiplate compressors, etc . In addition to a full field based on 2D-xy dimensions, a radially-symmetric scheme is also implemented, which relies on the Hankel transform. This reduces the system by one dimension, significantly releasing the memory constraint of the 3D $(x,y,t/\omega)$ field due to the use of a radially-symmetric $(r,t/\omega)$ field. Both solids and gas-based simulations are implemented; however, gas simulations are implemented only in the radially-symmetric scheme. Gas implementations include both noble and Raman-active gases. Not only scalar but also polarized fields can be simulated. The package exhibits an adaptive control of the step size. In addition to CPU, highly parallelized cuda computation with a Nvidia GPU is implemented. The package uses "RK4IP" (Runge-Kutta in the interaction picture) [1, 2].

The fastest way to learn how to use this code is to start with the example codes in the package.

1.2 Mathematical background

This package aims to solve the 3D unidirectional pulse propagation equation (3D-UPPE):

$$\partial_z \vec{\mathbb{A}}(\vec{k}_\perp, z, \Omega) = i \left[K_z - \left(\beta_{(0)} + \beta_{(1)}\Omega \right) \right] \vec{\mathbb{A}}(\vec{k}_\perp, z, \Omega)$$

$$+ i\frac{1}{2k_\omega} \left(1 + \frac{\left|\vec{k}_\perp\right|^2}{2k_\omega^2} \right) \mathfrak{F}_{k_\perp} \left[k_W^2(\vec{r}_\perp, \omega)\vec{\mathbb{A}}(\vec{r}_\perp, z, \Omega) \right]$$

$$+ i\frac{\omega^2}{2k_\omega c^2} \left(1 + \frac{\left|\vec{k}_\perp\right|^2}{2k_\omega^2} \right) \frac{\vec{P}(\vec{k}_\perp, z, \Omega)}{\epsilon_0}, \tag{1.1}$$

where $\vec{\mathbb{A}}$ is the field envelope (in $\sqrt{\mathrm{W/m^2}}$), with $\vec{\mathbb{A}}(\vec{k}_\perp) = \mathfrak{F}_{k_\perp}\left[\vec{\mathbb{A}}(\vec{r}_\perp)\right] = \mathfrak{F}_{k_x}\left[\mathfrak{F}_{k_y}\left[\vec{\mathbb{A}}(\vec{r}_\perp)\right]\right]$ representing the spatial frequency component after the spatial Fourier transform $[\mathfrak{F}_{k_x}[A](k_x) = C_{\mathfrak{F}_{k_x}}\int_{-\infty}^{\infty}A(x)\mathrm{e}^{-ik_x x}\,\mathrm{d}x$ and $\vec{r}_\perp = (x,y)]$, and $\vec{\mathbb{A}}(\Omega) = \mathfrak{F}\left[\vec{\mathbb{A}}(T)\right]$ representing the spectral component after spectral Fourier transform. Note that the spectral Fourier transform follow a different convention from that in mathematics due to following $(k_z z - \omega t)$. Due to the second-order spatial derivative in $\vec{r}_\perp$, the convention of spatial Fourier transform $\mathfrak{F}_{k_\perp}$ does not affect the result. To be consistent with K_z, we choose the convention of spatial Fourier transform such that it follows the same convention as that in mathematics, opposite to the spectral Fourier transform. The spectral Fourier transform is applied with respect to $\Omega = \omega - \omega_0$, where ω_0 is the center frequency of the numerical frequency window. $K_z(\vec{k}_\perp, \Omega) = \sqrt{k_\omega^2(\omega) - \left|\vec{k}_\perp\right|^2}$ represents both the (spectral) dispersion (from k_ω), and the (spatial) diffraction [from $\vec{k}_\perp = (k_x, k_y)$] terms. $k_W^2(\vec{r}_\perp, \omega)$ determines the waveguide effect; it is zero if the medium is homogeneous. They are determined by splitting the material's $k^2(\vec{r}_\perp, \omega) = \omega^2\mu_0\epsilon_0\epsilon_r(\vec{r}_\perp, \omega)$ into its spatially-independent part $k_\omega^2(\omega)$ and spatially-dependent part $k_W^2(\vec{r}_\perp, \omega)$, where $k_\omega^2(\omega)$ dominates the frequency variation in $k^2(\vec{r}_\perp, \omega)$:

$$k^2(\vec{r}_\perp, \omega) = k_\omega^2(\omega) + k_W^2(\vec{r}_\perp, \omega). \tag{1.2}$$

Because the dispersion and diffraction operators $\hat{D}_{\mathrm{is}} + \hat{D}_{\mathrm{if}} \sim K_z$ are not commutable with the waveguide operator $\hat{W} \sim k_W^2(\vec{r}_\perp, \omega)$, this separation [Eq. (1.2)] reduces the error resulting from incommutableness due to the Baker–Campbell–Hausdorff formula [3]. $\beta_{(0)}$ and $\beta_{(1)}$ are to reduce the propagating global phase increment to facilitate simulations in which $\beta_{(1)}$ is the inverse group velocity of the moving reference frame that introduces the delayed time $T = t - \beta_{(1)}z$.

$\vec{P}(\vec{r}_\perp, z, \Omega) = \mathfrak{F}\left[\vec{P}(\vec{r}_\perp, z, T)\right]$ is the nonlinear term. In solids, it follows

$$P^i(\vec{r}_\perp, z, \Omega) = \frac{2\epsilon_0 n(\omega)n_2}{3}\mathfrak{F}\left[\sum_{j=x,y}\left\{(1-f_R)\left[\left(\mathbb{A}^j\right)^2\left(\mathbb{A}^i\right)^* + 2\left|\mathbb{A}^j\right|^2\mathbb{A}^i\right]\right.\right.$$

$$+ f_R\left\{f_a\left[3\mathbb{A}^i(T)\int_0^\infty h_a(\tau)\left|\mathbb{A}^j(T-\tau)\right|^2\mathrm{d}\tau\right]\right.$$

$$\left.\left.\left. + f_b\left[\mathbb{A}^j(T)\int_0^\infty \frac{3}{2}h_b(\tau)\left(\mathbb{A}^i(\mathbb{A}^j)^* + (\mathbb{A}^i)^*\mathbb{A}^j\right)(T-\tau)\mathrm{d}\tau\right]\right\}\right\}\right]$$

$$+ P_I^i(\vec{r}_\perp, z, \Omega), \tag{1.3}$$

Cornell University

(for $i = x, y$) which becomes

$$
\begin{aligned}
P(\vec{r}_\perp, z, \Omega) = 2\epsilon_0 n(\omega) n_2 \mathfrak{F} \Big[& (1 - f_R) \, C_{\text{pol}}^K |\mathbb{A}|^2 \mathbb{A} \\
& + f_R \mathbb{A}(T) \int_0^\infty \Big(f_a h_a + C_{\text{pol}}^{R_b} f_b h_b \Big)(\tau) \big| \mathbb{A}(T - \tau) \big|^2 \mathrm{d}\tau \Big] \\
& + P_I(\vec{r}_\perp, z, \Omega) \\
= 2\epsilon_0 n(\omega) n_2 \mathfrak{F} & \left[(1 - f_R) \, C_{\text{pol}}^K |\mathbb{A}|^2 \mathbb{A} + f_R \left[\Big[f_a h_a + C_{\text{pol}}^{R_b} f_b h_b \Big] * |\mathbb{A}|^2 \right] \mathbb{A} \right] \\
& + P_I(\vec{r}_\perp, z, \Omega)
\end{aligned}
\tag{1.4}
$$

for scalar (singly-polarized) fields. n_2 is the material nonlinear refractive index (in m^2/W). f_R is the Raman fraction representing the contribution of the Raman response of all nonlinearities where f_a and f_b are Raman fractions of the total Raman response for isotropic and anisotropic Raman responses, respectively ($f_a + f_b = 1$); $h_a(t)$ and $h_b(t)$ are isotropic and anisotropic Raman response functions [4, 5]. C_{pol}^K is 1 if linearly-polarized or 2/3 if circularly polarized; $C_{\text{pol}}^{R_b}$ is 1 if linearly polarized or 1/2 if circularly polarized.

Gases usually have a much larger nonlinear Raman contribution than solids. In addition, the concept of "Raman fraction" makes physical sense only when it is in the transient or steady state where Raman nonlinearity also contributes to the nonlinear phase as the electronic nonlinearity [6]. In solids, due to Raman's short (tens of femtoseconds) dephasing time, this is almost always true, justifying the use of Raman fraction. However, this is not true in gases which usually exhibit hundreds-of-picosecond or nanosecond dephasing time. As a result, gas's nonlinear term follows [6]

$$
\begin{aligned}
P^i(\vec{r}_\perp, z, \Omega) = \frac{2\epsilon_0 n(\omega) n_2}{3} \mathfrak{F} & \left[\sum_{j=x,y} \left[\left(\mathbb{A}^j \right)^2 \left(\mathbb{A}^i \right)^* + 2 \big| \mathbb{A}^j \big|^2 \mathbb{A}^i \right] \right] \\
+ \frac{1}{\epsilon_0 n(\omega) c} \mathfrak{F} & \left[\sum_{j=x,y} \left[2\mathbb{A}^i(T) \int_0^\infty R_a(\tau) \big| \mathbb{A}^j(T - \tau) \big|^2 \mathrm{d}\tau \right.\right. \\
& \left.\left. + \mathbb{A}^j(T) \int_0^\infty R_b(\tau) \left(\mathbb{A}^i (\mathbb{A}^j)^* + (\mathbb{A}^i)^* \mathbb{A}^j \right)(T - \tau) \, \mathrm{d}\tau \right] \right] \\
+ P_I^i(\vec{r}_\perp, z, \Omega), &
\end{aligned}
\tag{1.5}
$$

(for $i = x, y$) which, in the scalar situation, becomes

$$
\begin{aligned}
P(\vec{r}_\perp, z, \Omega) = 2\epsilon_0 n(\omega) n_2 \mathfrak{F} & \left[C_{\text{pol}}^K |\mathbb{A}|^2 \mathbb{A} \right] \\
& + \frac{2}{\epsilon_0 n(\omega) c} \mathfrak{F} \left[\mathbb{A}(T) \int_0^\infty \Big(R_a + C_{\text{pol}}^{R_b} R_b \Big)(\tau) \big| \mathbb{A}(T - \tau) \big|^2 \mathrm{d}\tau \right] \\
& + P_I(\vec{r}_\perp, z, \Omega),
\end{aligned}
\tag{1.6}
$$

The gas Raman response functions are

$$
R_a = R^{\text{vib}} - 2R^{\text{rot}}
\tag{1.7a}
$$

$$
R_b = 6R^{\text{rot}},
\tag{1.7b}
$$

Cornell University

where

$$R^{\text{vib}} = \Theta(t) N_g \frac{\left(\frac{d\alpha}{d\mathbb{Q}}\right)_0^2}{4\mu} e^{-\gamma_2^{\text{vib}}t} \sum_J (2J+1)\, \rho_J^{(0)} \frac{1}{\omega_{1,J;0,J}} \sin\left(\omega_{1,J;0,J} t\right) \tag{1.8a}$$

$$R^{\text{rot}} = \Theta(t) N_g \frac{(\triangle\alpha)^2}{60\hbar} e^{-\gamma_2^{\text{rot}}t} \sum_J \left(\rho_J^{(0)} - \rho_{J+2}^{(0)}\right) \frac{(J+1)(J+2)}{(2J+3)} \sin\left(\omega_{0,J+2;0,J} t\right). \tag{1.8b}$$

$\Theta(t)$ is the Heaviside step function, $\left(\frac{d\alpha}{d\mathbb{Q}}\right)_0$ is the polarizability derivative at equilibrium, μ is the reduced mass of a molecule. γ_2^{vib} and γ_2^{rot} are dephasing rates of vibrational and rotational SRS, respectively. $\omega_{\nu_2,J_2;\nu_1,J_1} = \omega_{\nu_2,J_2} - \omega_{\nu_1,J_1}$ is the transition frequency of state (ν_1, J_1) to (ν_2, J_2). ν and J are the vibrational and rotational quantum numbers, respectively.

$\vec{P}_I(\vec{r}_\perp, z, \Omega)$ is the photoionization term that follows

$$\vec{P}_I(\Omega) = -\frac{e^2}{\omega^2 m_e} \frac{(-i+\omega\tau_c)\,\omega\tau_c}{1+\omega^2\tau_c^2} \mathfrak{F}\left[\rho_e(t)\vec{\mathbb{A}}(t)\right] + i\frac{E_b\epsilon_0 n_{\text{eff}}c}{\omega} \mathfrak{F}\left[\frac{\partial\rho_e}{\partial t} \frac{\vec{\mathbb{A}}(t)}{\left|\vec{\mathbb{A}}(t)\right|^2}\right], \tag{1.9}$$

whose electron density $\rho_e(t)$ is calculated with

$$\rho_e(t) \approx e^{\int_{-\infty}^t P_{\text{int}}(s)\,ds} \int_{-\infty}^t W(\tau) N_g e^{\int_{-\infty}^\tau -P_{\text{int}}(s)\,ds}\,d\tau \quad, \rho_e(t\to-\infty) = 0. \tag{1.10}$$

where $P_{\text{int}}(t) = -W(t) + \frac{\sigma_{IB}}{E_b}\left|\vec{\mathbb{E}}(t)\right|^2 - \frac{1}{\tau_r}$ is the integrating factor in solving the photoionization rate equation Eqs. (10.32) and (10.40). σ_{IB} is the cross section of the inverse Bremsstrahlung [Eq. (10.33)]. From the Perelomov-Popov-Terent'ev (PPT) model, the ionization rate $W_{\text{AC}}^{\text{PPT}}(t)$ for gases follows

$$W_{\text{AC}}^{\text{PPT}}(t) = \sum_m \left|C_{n^*,\ell^*}\right|^2 f(\ell,m) \frac{E_b}{\hbar} \sqrt{\frac{6}{\pi}} \left(\sqrt{\frac{\epsilon_0 n_{\text{eff}}c}{2}} \frac{\kappa}{\left|\vec{\mathbb{A}}(t)\right|\sqrt{1+\gamma(t)^2}}\right)^{2n^*-|m|-3/2}$$
$$\times A_m(\gamma(t)) e^{-\sqrt{\frac{\epsilon_0 n_{\text{eff}}c}{2}} \frac{\kappa}{3\left|\vec{\mathbb{A}}(t)\right|} g(\gamma(t))}, \tag{1.11}$$

whose Keldysh parameter $\gamma(t)$ and ponderomotive energy $U_p(t)$ follow

$$\gamma(t) = \sqrt{\frac{E_b}{2U_p(t)}} \quad, U_p(t) = \frac{e^2\left|\vec{\mathbb{A}}(t)\right|^2}{2m_e\left[\omega(t)\right]^2 \epsilon_0 n_{\text{eff}}c}. \tag{1.12}$$

On the other hand, the ionization rate for solids follows [29]:

$$W(t) = \frac{1}{N_e} \frac{2\omega}{9\pi} \left(\frac{\omega m_e}{\hbar\sqrt{\Gamma}}\right)^{3/2} Q(\gamma', x) e^{-\alpha\lceil x\rceil}, \tag{1.13}$$

The photoionization model is implemented in gases (*e.g.*, all noble gases, H_2, N_2, and O_2) and solids (*e.g.*, silica).

Cornell University

Chapter 2

Before I go deeply into details

2.1 Introduction

This document describes how to use the UPPE3D_propagate() MATLAB function.

Below is how to call this function in general.

```
1  prop_output = UPPE3D_propagate(fiber, ...
2                                  initial_condition, ...
3                                  sim, ...
4                                  [gas])
```

prop_output
    It contains the information of the output field after propagating through the medium, such as the field amplitudes and the positions of each saved field, etc.

fiber
    It contains the information of the fiber, such as the index profile.

initial_condition
    It contains the information of the input.

sim
    It contains a multitude of information about the simulation, such as the algorithm to use and the center wavelength, etc.

gas
    It contains the information required to run gas simulations, such as gas nonlinear refractive index and the information of its Raman response functions.

Chapter 3

Input arguments

Below, I use N_t as the number of time/frequency sampling points, N_x and N_y as the number of spatial sampling points in x and y dimensions, respectively. N_r is the number of spatial (radial) sampling points if the simulation employs its radially-symmetric scheme. N_p is the number of polarizations. N_z is the number of saved fields after the propagation. Overall, the dimension of simulation arrays follows $N_t \times N_x \times N_y \times N_z \times N_p$ in the xy scheme or $N_t \times N_r \times N_z \times N_p$ in the radially-symmetric scheme.

I recommend to use the information below as a reference guide if you're confused. Start with an example script is always better than reading this first.

Some parameters are required only when you enable some settings. Below I labeled in blue the parameters required all the time.

3.1   fiber

When I first learned fiber optics and began to developed all my code, I stored all information in the "fiber" structure. Here, this convention is kept, so "fiber" here in the 3D-UPPE is simply a MATLAB structure that stores all material properties.

fiber

This specifies the fiber type. It is used only with the index-creating function "calc_index_profile()," so in general, this parameter is not required depending on simulations.

n

This is the index profile of the medium. Its size is $N_t \times N_x \times N_y \times 1 \times N_p$ or $N_t \times N_r \times 1 \times N_p$ in the radially-symmetric scheme.

It can be used with the "calc_index_profile_i()" (i= "xy," or "r" for the radially-symmetric scheme) function to generate the index profile of fibers. For bulk crystals, just set it to a single-column frequency-dependent array (size: $N_t \times 1$) or a scalar to create a spatially-homogeneous index profile.

Below is the comment of "calc_index_profile_xy():"

```
1  %CALC_INDEX_PROFILE_XY It calculates the 2D index profile of the fiber.
2  %
3  %   fiber: a structure with
4  %
5  %       Below you can use the fiber in the repository (in "fiber_collections.m")
```

```
 6  %          or set all parameters yourself
 7  %          (1) Set it yourself
 8  %              fiber_type - a string with either "step', 'Nufern', or 'GRIN'
 9  %              material - fiber material; usually 'silica'
10  %              diameter - fiber core diameter (um)
11  %              NA - numerical aperture
12  %              extra_params - extra parameters for different fiber types
13  %
14  %          (2) Use fiber repository
15  %              fiber - the name of the fiber
16  %                      Currently I have '1060XP',
17  %                                       'YB1200-4_125',
18  %                                       'YB1200-6_125DC', 'YB1200-6_125DC-PM',
19  %                                       'YB1200-10_125DC', 'YB1200-10_125DC-PM',
20  %                                       'YB1200-20_400DC',
21  %                                       'YB1200-25_250DC', 'YB1200-25_250DC-PM',
22  %                                       'ER30-4_125', 'ER110-4_125',
23  %                                       'ER16-8_125', 'ER80-8_125',
24  %                                       'M5-980-125', 'M12-980-125',
25  %                                       'OM1', 'OM2', 'OM3', 'OM4',
26  %                                       'FUD-7005',
27  %                                       'PLMA-YDF-30_400-VIII'.
28  %
29  % ——————————————————————————————————
30  % (1) step fiber:
31  %      extra_params = [];
32  % (2) GRIN fiber:
33  %      extra_params.alpha = 2.08; % Shape parameter
34  % ——————————————————————————————————
35  %
36  %    Nx - number of spatial grid points
37  %    spatial_window - full spatial window size (um) (usually set to 100 um)
38  %    f - (Nt,1); frequency points (from small to large) (THz)
```

The operation is similar for the radially-symmetric "calc_index_profile_r():"

```
1  function index_profile = calc_index_profile_r(fiber,r,f)
2  %CALC_INDEX_PROFILE_R It calculates the 2D radially-symmetric index profile
3  % of the fiber. Only 1D radial information is generated.
4  %
5  ......
6  %
7  %    r - (1,Nr); radial sampling positions (m)
8  %    f - (Nt,1); frequency points (from small to large) (THz)
```

n2

    It's the nonlinear coefficient of the fiber. By default, UPPE3D_propagate() uses $2.3 \times 10^{-20} \, \text{m}^2/\text{W}$ assuming we use a silica fiber around $1 \, \mu\text{m}$ if fiber.n2 is left empty.

L0

    This is the fiber length. The unit is meter.

material

    This specifies the fiber material. It's 'silica' by default. It's used only for specifying which Raman model to use. It's either 'silica', 'chalcogenide', or 'ZBLAN'.

3.2   initial_condition

dt

    This is the time sampling step $\triangle t$ with a unit of ps.

Cornell University

For the xy scheme,

dx

This is the spatial sampling step $\triangle x$ with a unit of m.

dy

This is the spatial sampling step $\triangle y$ with a unit of m.

field

This is the temporal amplitude of the input field ($\mathbb{A}(t)$ with the unit $\sqrt{W/m^2}$). Its size is $N_t \times N_x \times N_y \times 1 \times N_p$.

If its size is $N_t \times N_x \times N_y \times N_z \times N_p$, only the last N_z is taken as the input field.

For the radially-symmetric scheme,

r

This is the radial sampling points with a unit of m. In the Hankel transform with high accuracy (FHATHA), the spatial radial dimension is sampled non-uniformly, following an exponential sampling strategy with denser sampling around the center [Eqs. (6.11) and (6.12)].

field

This is the temporal amplitude of the input field ($\mathbb{A}(t)$ with the unit $\sqrt{W/m^2}$). Its size is $N_t \times N_r \times 1 \times N_p$.

If its size is $N_t \times N_r \times N_z \times N_p$, only the last N_z is taken as the input field.

3.3   sim

Below are the most basic parameters for a simulation.

betas

In UPPE, we not only create a moving frame that follows the pulse with the inverse velocity $\beta_{(1)}$ but extract out the reference propagation constant $\beta_{(0)}$. The benefit of extracting $\beta_{(0)}$ is that it reduces the rate of global phase increment such that the simulation can run with a larger step. This is similar to the limitation of multimode simulations that different spatial modes have different propagation constants that generate beating. To resolve the multimode beating, the size of the z-step cannot be too large.

This "betas" is a 2×1 column vector.

$$\begin{bmatrix} \beta_{(0)} \\ \beta_{(1)} \end{bmatrix} \tag{3.1}$$

f0

The center frequency (THz). It's a scalar.

Cornell University

13

save_period

> The length between saved fields (m). If it's zero, it's equivalent to save_period=fiber.L0 that saves only the input and output fields.
>
> Be aware that this number needs to be a divisor of the fiber length, fiber.L0; otherwise, UPPE3D_propagate() will throw an error. I have the maximum step size set as the $\frac{1}{10}$ of the save_period and the position of the saved fields will be chosen as the one that first passes through each saved point.

3.3.1 Polarization modes

Here are the parameters if the simulation includes polarization modes.

scalar

> false (0) includes polarization-mode coupling
> true (1) don't include polarization-mode coupling

ellipticity

> The ellipticity of the polarization modes. Please refer to "Nonlinear Fiber Optics, Eq. (6.1.18) Agrawal" for the equations.
>
> 0 linear polarization (+,-)=(x,y)
> 1 circular polarization (+,-)=(right,left)

3.3.2 Adaptive-step method

Here are the parameters for the adaptive-step method which this code always uses. All parameters are contained within a "sim.adaptive_dz" structure. The user doesn't need to specify whether to use adaptive-step method or not; the code determines itself. With the adaptive-step method, the initial step size is set to a small 10^{-6} m.

adaptive_dz.threshold

> The nonlinear threshold of the upper-level adaptive-step method (see Ch. 8). It controls the accuracy of the simulation and determines whether to increase or decrease the step size. I typically use 10^{-6}.

adaptive_dz.DW_threshold

> The dispersion+diffraction threshold of the nested adaptive-step method (see Ch. 8). It controls the accuracy of the simulation and determines whether to increase or decrease the step size. I typically use 10^{-6}.

adaptive_dz.max_dz

> The maximum z-step size (m) of the adaptive-step method. It's 1/10 the save_period by default.

3.3.3 Hankel transform (FHATHA)

Here are the parameters required to run the radially-symmetric scheme. They are generated beforehand with the function "FHATHA_info()" and stored in the "FHATHA" stucture for simulations as

Cornell University

FHATHA.r

The radial sampling points with a unit of m [Eq. (6.10b)]. Its dimension is $(1, N_r)$.

FHATHA.kr

The radial sampling points in $k_\perp$-space with a unit of $2\pi/\text{m}$ [Eq. (6.10b)]. Its dimension is $(1, N_r)$.

FHATHA.dr

The radial sampling spacing with a unit of m. Its dimension is $(1, N_r - 1)$.

FHATHA.dkr

The radial sampling spacing in $k_\perp$-space with a unit of $2\pi/\text{m}$. Its dimension is $(1, N_r - 1)$.

FHATHA.l0

The ℓ_0 scalar constant used in FHATHA [Eq. (6.15)].

FHATHA.exp_prefactor

The exponential prefactor in P or R in FHATHA [Eq. (6.20a)].

FHATHA.r2_prefactor

The $(r_{\perp,n+1}^2/2)$ prefactor in P or R in FHATHA [Eq. (6.24)].

FHATHA.ifftQ

The $\mathfrak{F}^{-1}[Q]$ parameter in FHATHA [Eq. (6.20b)].

FHATHA.energy_restoration

Control the energy-restoration capability of the FHATHA algorithm. For details, see Chap. 6.2. Unless the propagation is very long or the energy conservation is strictly required, it is recommended to disable this for the highest computational performance.

true (1)	turn on energy restoration "during" propagation
false (0)	turn off energy restoration "during" propagation.
	Energy restoration is employed only at the beginning and the end of propagation.

3.3.4   Algorithm to use

gpu_yes

true (1)	use GPU
false (0)	don't use GPU

include_Raman

false(0)	ignore Raman effect
true(1)	Raman model including the anisotropic contribution
	("Ch. 2.3, p. 43" and "Ch. 8.5, p. 340," Nonlinear Fiber Optics (5th), Agrawal)

Typically, only isotropic Raman is considered, which is based on a single vibrational Raman mode of molecules (Ch. 2.3, p.42, Nonlinear Fiber Optics (5th), Agrawal). Here, we include the anisotropic part if there is an existing model, such as the one in silica ("Ch. 2.3, p. 43" and "Ch. 8.5, p. 340," Nonlinear Fiber Optics (5th), Agrawal).

Cornell University

For more details about anisotropic Raman, please read "Raman response function for silica fibers," by Q. Lin and Govind P. Agrawal (2006). Besides silica, chalcogenide and ZBLAN are also included.

photoionization_model

Photoionization model is implemented currently only for linearly-polarized fields.

true (1)	include the photoionization effect
false (0)	ignore the photoionization effect

pulse_centering

Because the pulse will evolve in the fiber, it's hard to have the moving frame always move with the same speed as the pulse. As a result, the pulse will go out of the time window and come back from the other side due to the use of periodic assumption of discrete Fourier transform. The shift in time is saved in "prop_output.t_delay" so that you don't lose the information

When enabling pulse_centering, the pulse will be centered to the center of the time window based on the moment of the field intensity ($|A|^2$).

true (1)	center the pulse according to the time window
false (0)	don't center the pulse

cuda_dir_path

The path to the cuda directory into which ptx files will be compiled and stored. This is "/UPPE3D/cuda/."

gpuDevice.Index

The GPU to use. It's typically 1 if the computer has only one GPU. MATLAB starts the index with 1. By starting multiple MATLAB sessions, we can run simulations on different GPUs simultaneously if different sessions are set with different GPU indices here.

Here are the parameters for the progress bar used in the simulation. It's useful in general to see how a simulation progresses.

progress_bar

true (1)	show progress bar
false (0)	don't show progress bar

progress_bar_name

The name of the GMMNLSE shown on the progress bar. If not set (no "sim.progress_bar_name"), it uses a default empty string, ".

Cornell University

Chapter 4

Output arguments

field
> The $N_t \times N_x \times N_y \times N_z \times N_p$ output field.

dt
> This is the time sampling step $\triangle t$ with a unit of ps.

z
> This is the positions of each saved field.

dz
> The z-step size (m).
>
> This contains the step size at each saved point. You can see how the step size evolves through the propagation with this parameter.

betas
> The "sim.betas," $[\beta_{(0)}; \beta_{(1)}]$, used in this propagation.

t_delay
> The time delay of the pulse at each saved point due to pulse centering.

seconds
> The time spent for this simulation.

_____

For the xy scheme,

dx
> This is the spatial sampling step $\triangle x$ with a unit of m.

dy
> This is the spatial sampling step $\triangle y$ with a unit of m.

....

For the radially-symmetric scheme,

r

This is the radial sampling points with a unit of m. In the Hankel transform with high accuracy (FHATHA), the spatial radial dimension is sampled non-uniformly, following an exponential sampling strategy with denser sampling around the center [Eqs. (6.11) and (6.12)].

Cornell University

Chapter 5

load_default_UPPE3D_propagate()

Because of the overwhelming parameters of input arguments, I've created a function that loads the default value for each parameter. If a user has specified the value already, the user's value precedes over the default one.

Here is a typical way of calling this function.

```
[ fiber , sim ] = load_default_UPPE3D_propagate ( input_fiber ,...
                                        input_sim ])
```

input_fiber and input_sim are user-defined parameters. Below are some examples.

```
% User−defined parameters
fiber.L0 = 3; % m

% Incorporate default settings
[ fiber , sim ] = load_default_UPPE3D_propagate ( fiber ,[] ) ;

% If there are "sim" settings
sim.gpu_yes = false ;
[ fiber , sim ] =  load_default_UPPE3D_propagate ( fiber , sim ) ;

% Use only user−defined "sim", not "fiber"
[ fiber , sim ] = load_default_UPPE3D_propagate ( [] , sim ) ;
```

Besides loading the default values, this function gives a user more options to obtain several parameters. This function transforms them into the allowed parameters of UPPE3D_propagate(). I list them below. If both equivalence are specified unfortunately, the allowed UPPE3D_propagate() input has the higher priority.

Description	Allowed UPPE3D_propagate()'s input	Equivalent input arguments for this function
center frequency/wavelength	sim.f0 (THz)	sim.lambda0 (m)

Below is the process flow of this "load_default_UPPE3D_propagate()" function. Read this if you're not sure whether your input will be used or overwritten. Because user-defined parameters take precedence, overwritten should happen only for (f0,lambda0) mentioned above.

```
% <−− Uncorrelated parameters are loaded directly −−>

sim.f0 − depend on input f0 or lambda0
```

```matlab
4            If no input f0 or lambda0, f0=3e5/1030e-9 (THz)

6  % If there's a user-defined one, use user's instead for the parameters below.
7  % Below I list the default values -->
8  fiber.fiber = '1060XP';
9  fiber.material = 'silica';
10 fiber.n2 = 2.3e-20;

12 sim.save_period = 0;

14 sim.ellipticity = 0; % linear polarization
15 sim.scalar = true;

17 sim.adaptive_dz.DW_threshold = 1e-6;
18 sim.adaptive_dz.threshold = 1e-6;

20 sim.gpu_yes = true;
21 sim.pulse_centering = true;
22 sim.include_Raman = true;
23 sim.gpuDevice.Index = 1;
24 sim.progress_bar = true;
25 sim.progress_bar_name = '';
26 sim.cuda_dir_path = 'UPPE3D/cuda';
```

Cornell University

Chapter 6

Radially-symmetric system

In scenarios that require a full-field simulation, pulse propagation most likely exhibits radial symmetry, such as in a multipass cell and a multiplate compressor. Although I develop this code initially for simulating nonlinear propagation in a multimode fiber that follows a non-radially-symmetric propagation, it can be useful to develop its radially-symmetric version for other uses.

6.1 Introduction

To develop the radially-symmetric version of the code, it is crucial to first introduce the Hankel transform, which naturally appears in the two-dimensional Fourier transform [7] of a radially-symmetric function:

$$
\begin{aligned}
A(k_\perp) = \mathfrak{F}_{k_\perp}[A(\vec{r}_\perp = r_\perp)] &\equiv C_\mathfrak{F}^2 \int_{-\infty}^{\infty} \int_{-\infty}^{\infty} A(r_\perp) e^{ic_s(k_x x + k_y y)} \, \mathrm{d}x \, \mathrm{d}y \\
&= C_\mathfrak{F}^2 \int_0^{2\pi} \int_0^{\infty} A(r_\perp) e^{ic_s|\vec{k}_\perp||\vec{r}_\perp|\cos\theta} |\vec{r}_\perp| \, \mathrm{d}|\vec{r}_\perp| \, \mathrm{d}\theta \quad , \vec{k}_\perp \cdot \vec{r}_\perp = \left|\vec{k}_\perp\right||\vec{r}_\perp|\cos\theta \\
&= C_\mathfrak{F}^2 \int_0^{\infty} A(r_\perp)|\vec{r}_\perp| \left(\int_0^{2\pi} e^{ic_s|\vec{k}_\perp||\vec{r}_\perp|\cos\theta} \, \mathrm{d}\theta \right) \mathrm{d}|\vec{r}_\perp| \\
&= 2\pi C_\mathfrak{F}^2 \int_0^{\infty} A(r_\perp) J_0(|c_s|k_\perp r_\perp) r_\perp \, \mathrm{d}r_\perp \\
&\equiv 2\pi C_\mathfrak{F}^2 \mathfrak{H}[A](k_\perp) \quad \because |c_s| = 1,
\end{aligned}
\tag{6.1}
$$

where $J_0(z) = \frac{1}{2\pi} \int_0^{2\pi} e^{iz\cos\theta} \, \mathrm{d}\theta$ is employed. Notations are simplified with $k_\perp = \left|\vec{k}_\perp\right| = \left|(k_x, k_y)\right|$ and $r_\perp = |\vec{r}_\perp| = \left|(x, y)\right|$. Similarly, the inverse Fourier transform becomes

$$
\begin{aligned}
A(r_\perp) = \mathfrak{F}_{k_\perp}^{-1}[A(k_\perp)] &\equiv C_{\mathfrak{I}\mathfrak{F}}^2 \int_{-\infty}^{\infty} \int_{-\infty}^{\infty} A(k_\perp) e^{-ic_s(k_x x + k_y y)} \, \mathrm{d}k_x \, \mathrm{d}k_y \\
&= 2\pi C_{\mathfrak{I}\mathfrak{F}}^2 \int_0^{\infty} A(k_\perp) J_0(|c_s|k_\perp r_\perp) k_\perp \, \mathrm{d}k_\perp \\
&\equiv 2\pi C_{\mathfrak{I}\mathfrak{F}}^2 \mathfrak{H}^{-1}[A](k_\perp).
\end{aligned}
\tag{6.2}
$$

The minus sign in the exponent disappears due to the integral over a full 2π angle; as a result, the Hankel transform displays the same formulation whatever the Fourier-transform convention is. In general, Hankel transform is defined for $\nu \geq -1/2$; however, because we are more interested in using it to solve radially-symmetric systems, discussion is limited only to Hankel transform of order 0 (*i.e.*, $\nu = 0$). The Hankel transform of order 0 is defined as

$$
\begin{aligned}
A_H(k_\perp) = \mathfrak{H}[A(r_\perp)] &\equiv \int_0^\infty A(r_\perp) J_0(k_\perp r_\perp) r_\perp \, \mathrm{d}r_\perp \\
A(r_\perp) = \mathfrak{H}^{-1}[A_H(k_\perp)] &\equiv \int_0^\infty A_H(k_\perp) J_0(k_\perp r_\perp) k_\perp \, \mathrm{d}k_\perp.
\end{aligned}
\tag{6.3}
$$

With the orthogonality relation

$$
\int_0^\infty J_\nu(kr) J_\nu(k'r) r \, \mathrm{d}r = \frac{\delta(k - k')}{k}, \quad k, k' > 0,
\tag{6.4}
$$

Eq. (6.3) forms a Hankel-transform pair with $\mathfrak{H}\mathfrak{H}^{-1} = \mathfrak{H}^{-1}\mathfrak{H} = 1$. This relation can also be verified with one-dimensional $\mathfrak{F}\mathfrak{F}^{-1} = \mathfrak{F}^{-1}\mathfrak{F} = 1$ by noting that $C_\mathfrak{F} C_{\mathfrak{I}\mathfrak{F}} = \frac{1}{2\pi}$ with the following Fourier-transform representation:

$$
\mathfrak{F}_{k_\perp} = 2\pi C_\mathfrak{F}^2 \mathfrak{H}
\tag{6.5a}
$$

$$
\mathfrak{F}_{k_\perp}^{-1} = 2\pi C_{\mathfrak{I}\mathfrak{F}}^2 \mathfrak{H}^{-1}.
\tag{6.5b}
$$

Hankel transform satisfies a similar convolution theorem to the Fourier transform, which follows

$$
\mathfrak{H}[A * *B] = 2\pi \mathfrak{H}[A]\mathfrak{H}[B]
\tag{6.6a}
$$

$$
\mathfrak{H}^{-1}[A * *B] = 2\pi \mathfrak{H}^{-1}[A]\mathfrak{H}^{-1}[B],
\tag{6.6b}
$$

derived by applying Eq. (6.5) to the two-dimensional version of the Fourier-transform convolution theorem:

$$
\mathfrak{F}_{k_\perp}[A * *B] = \frac{1}{C_\mathfrak{F}^2} \mathfrak{F}_{k_\perp}[A]\mathfrak{F}_{k_\perp}[B],
$$

with $A * *B = \displaystyle\int_{-\infty}^\infty \int_{-\infty}^\infty A(x, y) B(X - x, Y - y) \, \mathrm{d}x \, \mathrm{d}y$ represents the two-dimensional convolution

$$
= \int_0^{2\pi} \int_0^\infty A(r) B(|\vec{R} - \vec{r}|) r \, \mathrm{d}r \, \mathrm{d}\theta, \text{ if } A \text{ and } B \text{ are radially symmetric}
$$

$\Rightarrow A * *B$ is also radially symmetric. (Fig. 6.1)

With Eq. (6.5a), it is transformed into Eq. (6.6a). A similar process can be applied to derive Eq. (6.6b).

Hankel transform satisfies the Parseval's theorem as well. The two-dimensional Parseval's theorem of the Fourier transform is

$$
\frac{1}{C_{\mathfrak{I}\mathfrak{F}}^2} \int_{-\infty}^\infty \int_{-\infty}^\infty \left| A(\vec{r}_\perp) \right|^2 \mathrm{d}x \, \mathrm{d}y = \frac{1}{C_\mathfrak{F}^2} \int_{-\infty}^\infty \int_{-\infty}^\infty \left| A(\vec{k}_\perp) \right|^2 \mathrm{d}k_x \, \mathrm{d}k_y.
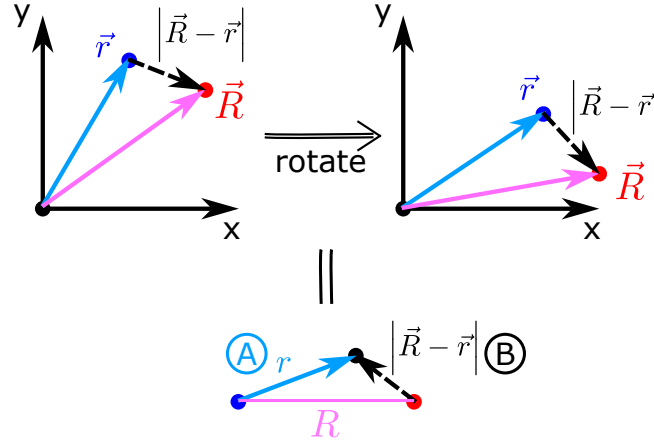\tag{6.7}
$$

Cornell University

Figure 6.1: Two-dimensional convolution $A**B$ of two radially-symmetric functions $A(r)$ and $B(r)$. Because A depends only on $\vec{r}$ and B only on $\left|\vec{R}-\vec{r}\right|$, the convolution $(A**B)(R) = \int_0^{2\pi}\int_0^\infty A(r)B(\left|\vec{R}-\vec{r}\right|)r\,\mathrm{d}r\,\mathrm{d}\theta$ is also radially symmetric. This convolution can be treated as multiplying values depending on the black dot moving over the entire space (bottom figure), whose only independent variable is the distance R between the blue and red dots.

If A is radially symmetric (and thus its 2D Fourier transform $A(\vec{k}_\perp)$ is also radially symmetric [Eq. (6.1)]), with Eq. (6.5a), it becomes

$$\frac{1}{C_{\mathfrak{F}\mathfrak{F}}^2}2\pi\int_0^\infty \left|A(r_\perp)\right|^2 r_\perp\,\mathrm{d}r_\perp = \frac{1}{C_{\mathfrak{F}}^2}2\pi\int_0^\infty \left|\left(2\pi C_{\mathfrak{F}}^2\right)A_H(k_\perp)\right|^2 k_\perp\,\mathrm{d}k_\perp, \tag{6.8}$$

which leads to the Parseval's theorem for the Hankel transform:

$$\int_0^\infty \left|A(r_\perp)\right|^2 r_\perp\,\mathrm{d}r_\perp = \int_0^\infty \left|A_H(k_\perp)\right|^2 k_\perp\,\mathrm{d}k_\perp. \tag{6.9}$$

6.2 Numerical computation: Fast Hankel transform of high accuracy (FHATHA)

In this section, we will discuss how to numerically compute the Hankel transform with the "fast Hankel transform of high accuracy," which Magni *et al.* abbreviated as FHATHA [8]. There are a few numerical procedures to compute the Hankel transform, among which one of the most popular is the quasi-fast Hankel transform (QFHT) [9, 10]. FHATHA outperforms QFHT by exhibiting two orders of magnitude lower error while relying on the well-established FFT that offers computational efficiency. However, it exhibits a problem with energy conservation. Further improvements need to be included, which is also discussed.

Cornell University
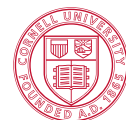
Magni's approach

In FHATHA, both the fields in real $\vec{r}_\perp$-space and $\vec{k}_\perp$-space follow an exponential sampling strategy:

$$r_{\perp,n} = r_\perp^{\max} \zeta_n \tag{6.10a}$$

$$k_{\perp,n} = k_\perp^{\max} \zeta_n, \tag{6.10b}$$

where ζ_n represents the normalized coordinate that follows

$$\zeta_n = \zeta_0 e^{\alpha n}, \quad n = 0, 1, \cdots, N_\perp - 1 \tag{6.11}$$

with $\zeta_0 = \frac{1+e^\alpha}{2} e^{-\alpha N_\perp}$ such that $\zeta_n, \forall n \geq 1$ are in the center of each interval $[\xi_n, \xi_{n+1}]$. ξ_n is the normalized coordinate following

$$\xi_n = \begin{cases} 0, & n = 0 \\ \xi_0' e^{\alpha n}, & n = 1, 2, \cdots, N_\perp \end{cases}, \tag{6.12}$$

where $\xi_0' = e^{-\alpha N_\perp}$ (Fig. 6.2). α is given such that the widths of the first and the last intervals are the same:

$$\xi_1 - \xi_0 = \xi_{N_\perp} - \xi_{N_\perp - 1}$$
$$\Rightarrow e^{-\alpha(N_\perp - 1)} = 1 - e^{-\alpha}, \tag{6.13}$$

which can be easily solved numerically. During computing the Hankel transform, the function needs to be evaluated at the center of each interval. However, ζ_0 is not at the center of $[\xi_0, \xi_1]$, as we redefine ξ_0 from ξ_0' to 0 [Eq. (6.12)]. Therefore, $A(r_{\perp,0} = r_\perp^{\max} \zeta_0)$ needs to be replaced with $A(r_{\perp,0}' = r_\perp^{\max} \zeta_0')$ (with $\zeta_0' = \xi_1/2$ being at the center of $[\xi_0 = 0, \xi_1]$), which is approximated through extrapolation of $A(r_{\perp,0})$ and $A(r_{\perp,1})$ with a parabola with zero derivative at the origin, a reasonable approximation curve for a radially-symmetric function. In FHATHA, an additional evaluation is required at $\zeta_{N_\perp}$, beyond the range of Eq. (6.11), which is simply treated with $A(r_{\perp,N_\perp} = r_\perp^{\max} \zeta_{N_\perp}) = 0$. If we denote A_n as $A(r_{\perp,n})$, eventually the A that is used in FHATHA is

$$\tilde{A}_n = \begin{cases} A(r_{\perp,0}') = \ell_0 (A_0 - A_1) + A_1, & n = 0 \\ A_n, & n = 1, 2, \cdots, N_\perp - 1 \\ 0, & n = N_\perp \end{cases} \tag{6.14}$$

where

$$\ell_0 = \frac{e^\alpha (2 + e^\alpha)}{(1 + e^\alpha)^2 (1 - e^{-2\alpha})}. \tag{6.15}$$

FHATHA solves the Hankel transform by summing over Hankel-transform integral of each interval, whose function is evaluated at ζ_n [Eq. (6.11)] (with slight modification at $n = 0$ [Eq. (6.14)]) but interval is defined with ξ_n [Eq. (6.12)]:

$$\int_{r_\perp^{\max}\xi_n}^{r_\perp^{\max}\xi_{n+1}} A(r_\perp) J_0(k_\perp r_\perp) r_\perp \, \mathrm{d}r_\perp \approx \tilde{A}_n \int_{r_\perp^{\max}\xi_n}^{r_\perp^{\max}\xi_{n+1}} J_0(k_\perp r_\perp) r_\perp \, \mathrm{d}r_\perp$$

$$= \tilde{A}_n \frac{r_\perp}{k_\perp} J_1(k_\perp r_\perp) \Big|_{r_\perp^{\max}\xi_n}^{r_\perp^{\max}\xi_{n+1}}$$

$$= \frac{\tilde{A}_n}{k_\perp} \left[(r_\perp^{\max}\xi_{n+1}) J_1(k_\perp (r_\perp^{\max}\xi_{n+1})) - (r_\perp^{\max}\xi_n) J_1(k_\perp (r_\perp^{\max}\xi_n)) \right]$$

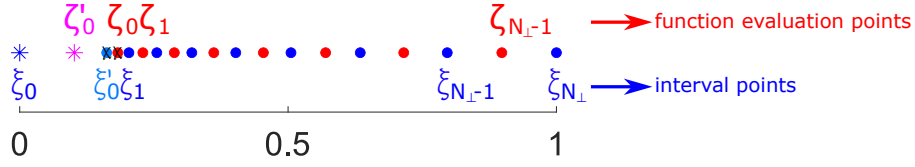$$\tag{6.16}$$

Cornell University

Figure 6.2: Numerical sampling in FHATHA.

by use of the relation $\int J_0(u)u\,\mathrm{d}u = uJ_1(u) + C$. Summing over all $n = 0, 1, \cdots, (N_\perp - 1)$ leads to

$$
\begin{aligned}
A_{H,m} = A_H(k_{\perp,m}) &= \frac{1}{k_{\perp,m}} \sum_{n=0}^{N_\perp - 1} \ell_n \left(A_n - A_{n+1} \right) \left(r_\perp^{\max} \xi_{n+1} \right) J_1(k_{\perp,m} \left(r_\perp^{\max} \xi_{n+1} \right)) \\
&= \frac{r_\perp^{\max}}{k_{\perp,m}} \sum_{n=0}^{N_\perp - 1} \left[\ell_n \left(A_n - A_{n+1} \right) \mathrm{e}^{\alpha(n+1-N_\perp)} \right] J_1(k_\perp^{\max} r_\perp^{\max} \zeta_0 \mathrm{e}^{\alpha(m+n+1-N_\perp)}),
\end{aligned}
\tag{6.17}
$$

where $\ell_n = 1$ if $n \neq 0$, and J_1 is the Bessel function of order 1.

If we define the discrete cross correlation $\star_D$ as

$$
(P \star_D Q)_m \equiv \sum_n \overline{P_n} Q_{m+n}.
\tag{6.18}
$$

It satisfies

$$
\begin{aligned}
\mathfrak{F}_D[P \star_D Q] &= \frac{1}{C_{\mathfrak{F}_D}} \overline{\mathfrak{F}_D[P]} \mathfrak{F}_D[Q] = \frac{1}{C_{\mathfrak{F}_D}} \left(\frac{C_{\mathfrak{F}_D}}{C_{\mathfrak{I}\mathfrak{F}_D}} \mathfrak{F}_D^{-1}[\overline{P}] \right) \mathfrak{F}_D[Q] \\
&= \frac{1}{C_{\mathfrak{I}\mathfrak{F}_D}} \mathfrak{F}_D^{-1}[\overline{P}] \mathfrak{F}_D[Q].
\end{aligned}
\tag{6.19}
$$

Since DFT inherently exhibits periodicity, zero-padding is required if P or Q does not display periodicity beyond the sampling window; otherwise, aliasing will occur by direct application of Eq. (6.19).

If we let

$$
P_n = \overline{R}_n = \begin{cases} \ell_n \left(\overline{A}_n - \overline{A}_{n+1} \right) \mathrm{e}^{\alpha(n+1-N_\perp)}, & n = 0, 1, \cdots, N_\perp - 1 \\ 0, & n = N_\perp, N_\perp + 1, \cdots, T_{\text{extended}}^w \quad \text{(zero-padding)} \end{cases}
\tag{6.20a}
$$

$$
Q_n = J_1(k_\perp^{\max} r_\perp^{\max} \zeta_0 \mathrm{e}^{\alpha(n+1-N_\perp)}), \qquad n = 0, 1, \cdots, T_{\text{extended}}^w
\tag{6.20b}
$$

Eq. (6.17) becomes

$$
A_{H,m} = \frac{r_\perp^{\max}}{k_{\perp,m}} \frac{1}{C_{\mathfrak{I}\mathfrak{F}_D}} \mathfrak{F}_D^{-1} \left[\mathfrak{F}_D^{-1}[R] \mathfrak{F}_D[Q] \right]
\tag{6.21a}
$$

$$
\overset{\text{or also}}{=\joinrel=} \frac{r_\perp^{\max}}{k_{\perp,m}} \frac{1}{C_{\mathfrak{F}_D}} \mathfrak{F}_D \left[\mathfrak{F}_D[R] \mathfrak{F}_D^{-1}[Q] \right],
\tag{6.21b}
$$

Cornell University

which is meaningful only for $m = 0, 1, \cdots, (N_\perp - 1)$ with others discarded after FHATHA. The zero-padding range is determined by $T^w_{\text{extended}} \geq 2N_\perp - 2$ [so that there are a total of $(2N_\perp - 1)$ sampling points]. This zero-padding procedure is similar to the convolution operation with clipped extended signals. However, since the summation in Eq. (6.17) includes Q_n up to $n = 2N_\perp - 2$, Q_n must be analytically computed at least for $n = 0, 1, \cdots, (2N_\perp - 2)$, rather than simple zero-padding as in the convolution theorem. Note that Q can be precomputed only once before the simulation. In the physical Fourier-transform convention ($C_{\mathfrak{F}_D} = \frac{1}{\mathfrak{N}}$ and thus $C_{\mathfrak{I}\mathfrak{F}_D} = 1$), $A_{H,m} = \frac{r_\perp^{\max}}{k_{\perp,m}} \mathfrak{F}_D^{-1} \left[\mathfrak{F}_D^{-1}[R] \mathfrak{F}_D[Q] \right]$, which is (in MATLAB syntax below)

```
1   A_H = r_max./k.*fft(fft(R).*ifft(Q));
```

Since Hankel transform and inverse Hankel transform exhibit the same form [Eq. (6.3)], inverse FHATHA follows Eq. (6.21) by swapping the symbols $r \leftrightarrow k$. Note that Q is independent of Hankel or inverse Hankel transforms due to its $(r_\perp, k_\perp)$ symmetry. Fig. 6.3 shows two verification examples that demonstrate its excellent consistency with the analytical formula.
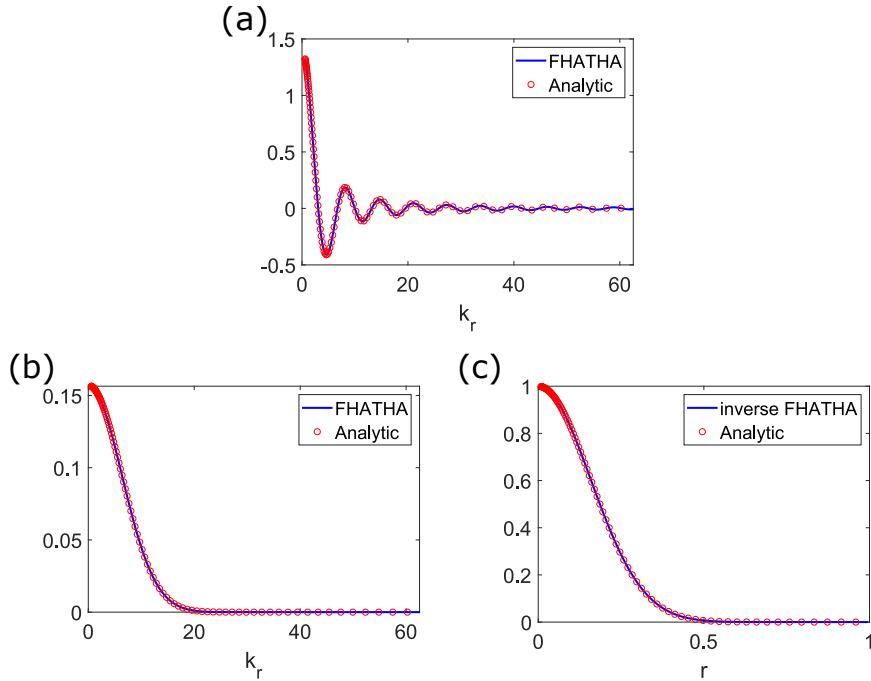

Figure 6.3: Verifications of FHATHA. Hankel transforms of (a) $f(r) = \sqrt{\frac{5}{2\pi}} r^2$ and (b) $f(r) = e^{-20r^2}$, which are $\sqrt{10\pi} \frac{2\eta J_0(\eta) + (\eta^2 - 4) J_1(\eta)}{\eta^3}$ (with $\eta = r_\perp^{\max} k_\perp$) and $\frac{\pi}{20} e^{-k_\perp^2/80}$, respectively. (c) Inverse Hankel transform of (b). This is used to further verify the operation of inverse Hankel transform and see whether the signal can be recovered.

The exponential sampling strategy [Eqs. (6.11) and (6.12)] of FHATHA introduces an advantage over typical uniform sampling. Mostly, the radially-symmetric field is the strongest at the spatial center. In particular, in cases such as self-focusing for a high-peak-power pulse (Fig. 6.4), the spatial extent of the field decreases as it propagates. This can lead to undersampling of the field, which is resolved by FHATHA's exponential sampling that densely samples around the center.

Unlike the frequency window in the Fourier transform that is determined by the temporal
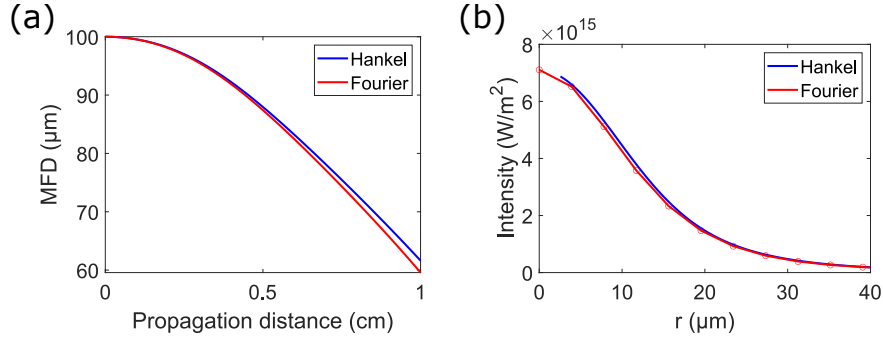
Cornell University

Figure 6.4: (a) Mode-field-diameter (MFD) evolution of a pulse propagating in a 1-cm-long bulk silica, simulated with the Hankel transform or 2D spatial Fourier transform. The input pulse is 1-ps-long and has 8-µJ pulse energy, with a Gaussian spatial profile of 100-µm MFD. (b) The intensity profile of the pulse.

sampling period, the $k_\perp$ window can be chosen quite arbitrarily. Its value is determined by the signal's maximum $k_\perp$.

Important steps to improve FHATHA for ultrafast pulse propagation

In fact, FHATHA proposed by Magni *et al.* requires modifications to be correctly employed in ultrafast pulse propagation. Because it does not satisfy any discrete Parseval's theorem as by the DFT, the FHATHA-transformed signal "numerically" does not conserve energy. Although FHATHA approximates the continuous Hankel transform with a (continuous) Parseval's theorem [Eq. (6.9)], it inherently suffers from energy non-conservation, which can be visualized through comparisons of signals after repetitive operations of FHATHA and inverse-FHATHA operations [Figs. 6.5(a) and (b) of both $N_\perp = 100$ and 1000].

To mitigate FHATHA's deviation due to a lack of energy conservation, energy restoration is added to the end of FHATHA:

```
1  % E0 and E_H are powers of the original and the transformed signals
2  % A is usually in "W/m^2", so E0 is in "W", the power.
3  E0 = 2*pi*trapz(r,abs(A).^2.*r);
4  E_H = 2*pi*trapz(kr,abs(A_H).^2.*kr);
5  % Energy restoration
6  A_H = A_H.*sqrt(E0./E_H);
```

The energy-restoration operation significantly improves FHATHA's accuracy when the number of sampling ($N_\perp$) is small [Figs. 6.5(c) and (d) in the blue box]. However, at large $N_\perp$, the root-mean-squared error (RMSE) increases with the energy restoration, compared with the one without it [Figs. 6.5(a–d) in the red box]. A reasonable speculation is that the simple energy-restoration operation proposed previously uniformly scales the transformed signal, which potentially modulates the weak (background) signal at the window edge and artificially induces an error. However, as shown in the simulation of a Gaussian field (Fig. 6.6), a lack of energy-restoration operation generates simulation results with varying energy.

Another reason for FHATHA's deviation is omission of signals at $r_\perp = 0$ and $k_\perp = 0$. In addition, the exponential sampling strategy [Eqs. (6.11) and (6.12)] induces a huge gap between the first sampling point and $r_\perp = 0$ (or $k_\perp = 0$). Magni *et al.* verified FHATHA with a parabolic signal that has a higher amplitude at larger $r_\perp$. This signal justifies FHATHA's approach of

Cornell University

approximating $A(r'_{\perp,0})$ with A_0 and A_1 [Eq. (6.14)]. However, in practical ultrafast optical applications, the beam exhibits a spatially-confined profile, usually Gaussian. FHATHA's sampling gap and $A(r'_{\perp,0})$ approximation easily induce a significant error for such a signal that is the strongest around the spatial (or $\vec{k}_\perp$-space) center. To resolve this, the signal at the center needs to be taken into account. Assume that the signal to be transformed includes sampling at $r_\perp = 0$, the numerical signal used in FHATHA [$\tilde{A}_n$ in Eq. (6.14)] is modified to be

$$
\tilde{A}_n = \begin{cases} A(r'_{\perp,0}) = \frac{1}{2}\left\{ \left[\ell_0\left(A_0 - A_1\right) + A_1\right] + \left(\frac{1}{1+e^\alpha}A_{-1} + \frac{e^\alpha}{1+e^\alpha}A_0\right)\right\}, & n = 0 \\ A_n, & n = 1, 2, \cdots, N_\perp - 1 \\ 0, & n = N_\perp \end{cases}
$$

$$(6.22)$$

which takes into account the signal at the spatial center, denoted as A_{-1}. $\left(\frac{1}{1+e^\alpha}A_{-1} + \frac{e^\alpha}{1+e^\alpha}A_0\right)$ is the approximate signal at $r'_{\perp,0}$ with known signals at $r_\perp = 0$ and $r_{\perp,0}$. With reasonably-fine sampling, $\alpha \approx 0.01$ or less, and thus the approximate signal approaches $(A_{-1} + A_0)/2$. The modified signal considers, at $r'_{\perp,0}$, the mean of signals from the original FHATHA's parabolic approximation and from the linear interpolation of A_{-1} and A_0. Thus, the Hankel-transform signal follows

$$
\begin{aligned}
A_{H,m} = A_H(k_{\perp,m}) &= \frac{1}{k_{\perp,m}} \sum_{n=0}^{N_\perp-1} \left(\tilde{A}_n - \tilde{A}_{n+1}\right)\left(r_\perp^{\max}\xi_{n+1}\right) J_1(k_{\perp,m}\left(r_\perp^{\max}\xi_{n+1}\right)) \\
&= \frac{r_\perp^{\max}}{k_{\perp,m}} \sum_{n=0}^{N_\perp-1} \left[\left(\tilde{A}_n - \tilde{A}_{n+1}\right) e^{\alpha(n+1-N_\perp)}\right] J_1(k_\perp^{\max}r_\perp^{\max}\zeta_0 e^{\alpha(m+n+1-N_\perp)}),
\end{aligned}
$$

$$(6.23)$$

for $m = 0, 1, \cdots, (N_\perp-1)$. Eq. (6.23) is subsequently solved with the FFT-based cross correlation [Eqs. (6.20) and (6.21)]. By employing the relation $\frac{r_\perp}{k_\perp}J_1(k_\perp r_\perp) \approx \frac{r_\perp^2}{2}$ (due to $J_1(x) \approx \frac{x}{2}$ for $0 \leq x \ll 1$), we can find the transformed signal at $k_\perp = 0$ through

$$
\begin{aligned}
A_{H,-1} = A_H(k_{\perp,-1} = 0) &= \sum_{n=0}^{N_\perp-1} \left(\tilde{A}_n - \tilde{A}_{n+1}\right)\frac{r_{\perp,n+1}^2}{2} \\
&= (r_\perp^{\max})^2 \sum_{n=0}^{N_\perp-1} \left(\tilde{A}_n - \tilde{A}_{n+1}\right)\frac{e^{2\alpha(n+1-N_\perp)}}{2}.
\end{aligned}
$$

$$(6.24)$$

The comparisons of Figs. 6.5(a,b) and (g,h) show that the inclusion of spatial and $\vec{k}_\perp$-space centers reduces FHATHA's error, with a significant amount at small $N_\perp$.

In conclusion, FHATHA requires additional steps of energy restoration and consideration of spatial and $\vec{k}_\perp$-space centers. Energy restoration (through a simple uniform scaling) can slightly distort the transformed signal but is a required step in simulations. On the other hand, consideration of spatial and $\vec{k}_\perp$-space centers only improves the result. In numerical pulse-propagation simulations, the field is usually solved in the $\vec{k}_\perp$ space through

$$
A(k_\perp, z + \mathrm{d}z, \omega) = A(k_\perp, z, \omega) + f(A(k_\perp, z, \omega), k_\perp, \omega)\,\mathrm{d}z, \tag{6.25}
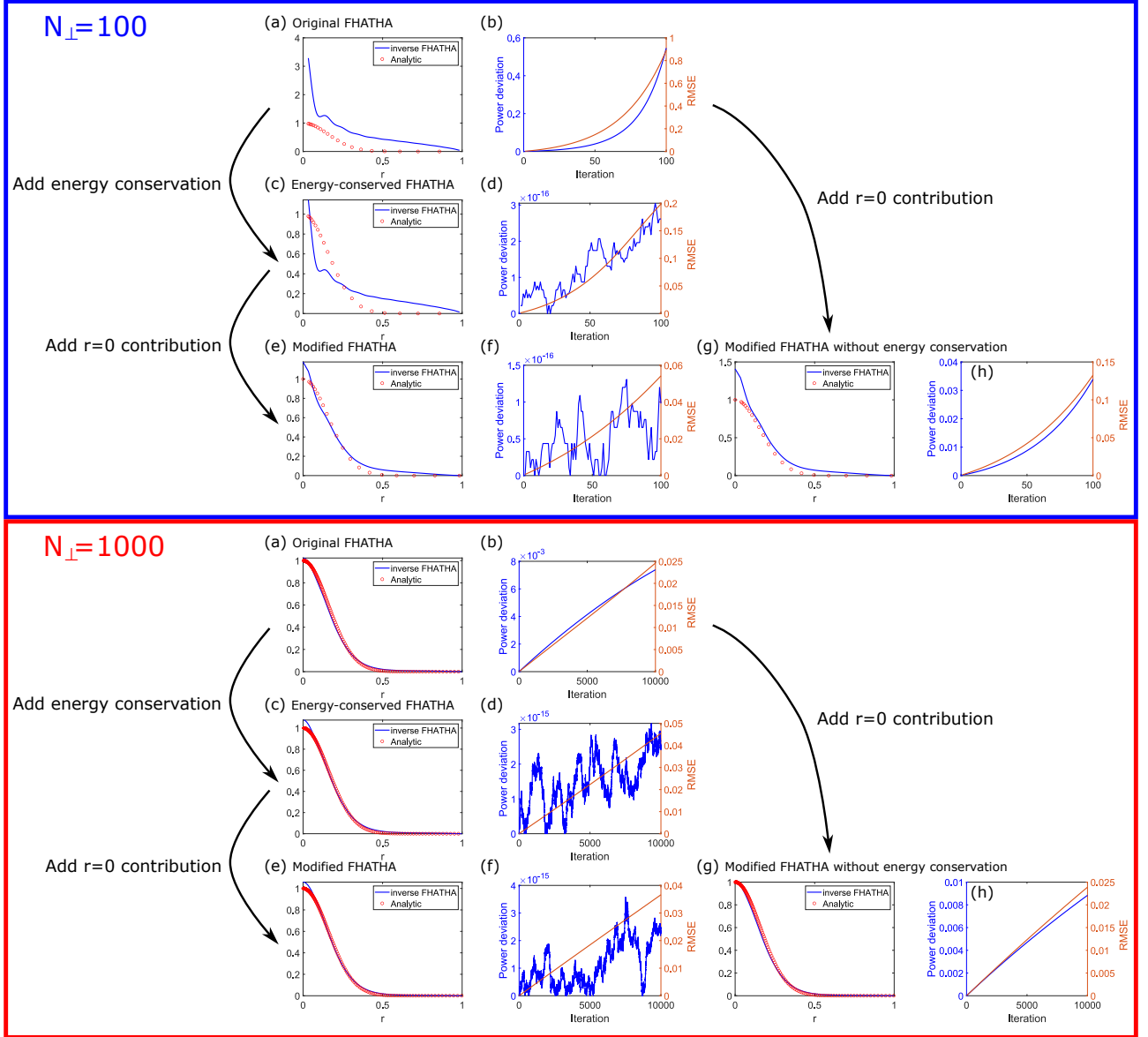$$

Cornell University

Figure 6.5: Comparisons of FHATHA with different modifications. (a), (c), (e), and (g) are spatial profiles of the FHATHA-transformed signals after many operations of (FHATHA,inverse FHATHA) pair, and its analytic results that follow the Gaussian profile in Fig. 6.3(b). (d), (f), and (h) are power $(2\pi \int_0^\infty |A|^2 r \, dr)$ deviations (blue) and root-mean-squared errors (orange) of two signals $(\sqrt{\frac{\sum_{n=1}^{N_\perp} |A_{\text{analytic}}(n) - A_H(n)|^2}{N_\perp}})$ with increasing iterations. Top (those in the blue box) and bottom (in the red box) are results with different numbers of sampling points.

where $(f \, dz)$ is effectively solved with various numerical stepping schemes, such as the Runge-Kutta. Solving f usually involves a few Hankel and inverse Hankel transforms. Since $|f \, dz|$ is generally small, FHATHA's error in energy does not significantly affect the propagating field, as seen in Fig. 6.6. The energy deviation occurs only in the first and last field transformations that transform the field to the $\vec{k}_\perp$ space to initiate the propagation and back to the $\vec{r}_\perp$ space when finished. As a result, energy-conserved FHATHA is applied only in the first and last
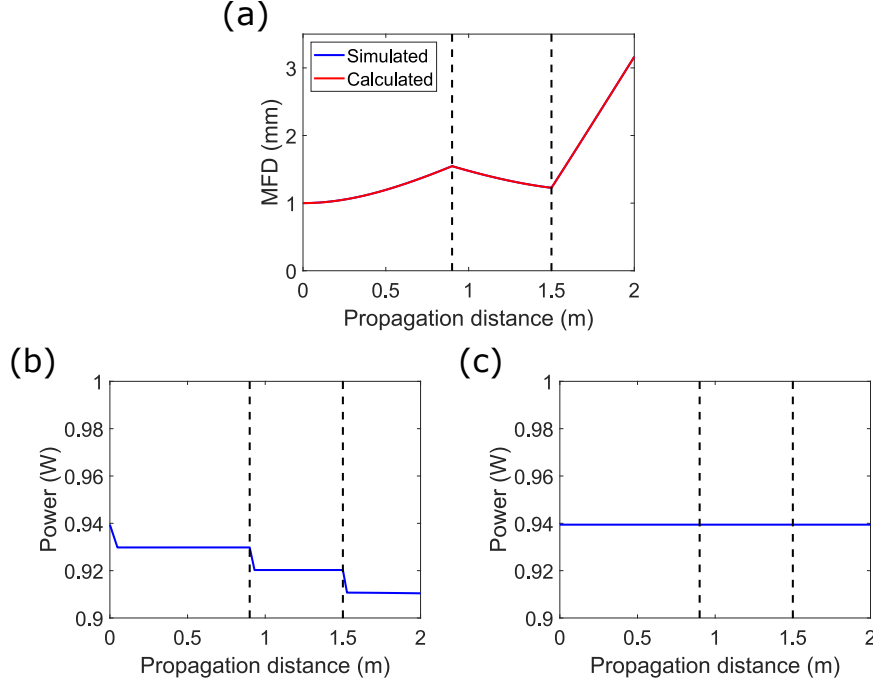
Figure 6.6: Numerical simulation of a Gaussian field propagating through a Galileo telescope with the first ($f = 0.9$ m) and the second ($f = -0.3$ m) lenses. This telescope increases the beam size by three times. (a) MFD evolution. The calculated red line is derived from typical ABCD matrices of a Gaussian field. Lines from simulations (blue) and ABCD matrices (red) perfectly overlap. (b) and (c) are total powers of the field during propagation without and with energy restoration in FHATHA, respectively. This simulation involves three separate field propagations between lenses. Lens effect is considered by adding a simple spatial lens phase to the field.

transformations, while the main optical propagation can employ FHATHA, with or without energy restoration depending on simulation conditions (Fig. 6.7). If the propagation distance is long or a simulation involves multiple propagations, energy restoration is recommended to avoid error accumulation; otherwise, it can be disabled for an improved computational performance and potentially higher transformation accuracy as described previously. In the meantime, space centers are always considered in FHATHA.

Cornell University

$$A(\vec{r}_\perp, z, \omega)$$

Hankel transform $\quad\downarrow\quad$ modified FHATHA with energy restoration

$$A(\vec{k}_\perp, z, \omega)$$

consider center points

Optical propagation $\quad$ modified FHATHA (with or without energy restoration)

inverse Hankel transform $\quad\downarrow\quad$ modified FHATHA with energy restoration
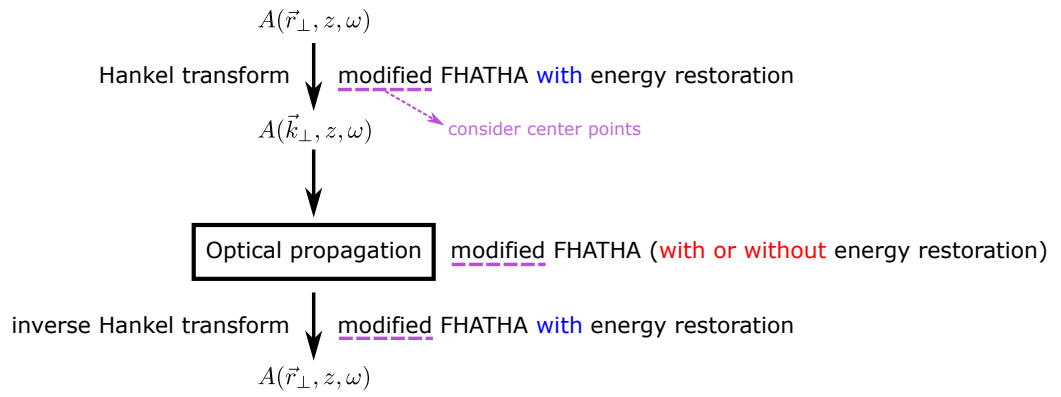
$$A(\vec{r}_\perp, z, \omega)$$

Figure 6.7: Optical propagation simulation scheme with the FHATHA-based Hankel transform. During optical propagation, whether to impose FHATHA's energy-restoration operation depends on the amount of potential error accumulation.

Cornell University

Chapter 7

Computation of gas

We have implemented a few gases (for "gas.material"): H_2, N_2, O_2, air, Xe, Ar, Ne, He, Kr, and CH_4. Raman models have been implemented for Raman-active gases: H_2, N_2, O_2, air, and CH_4. Photoionization has been implemented for all gases except air.

Follow the code below (the numeric values are chosen as examples. Modify them based on your needs.):

```
%% Configure gas parameters for the gas_info().
gas.temperature = 288; % Kelvin
gas.pressure = 1*1e5; % Pa
gas.material = 'Ar'; % use Ar gas

% Load fiber parameters based on the configured parameters
%
% gas.Ng - 1/m^3; gas number density
% gas.(gas.material).(Raman_type).(Raman_parameters)
[fiber,sim,gas] = gas_info(fiber,sim,gas,lambda*1e-9);
```

Chapter 8

Diagram of the calling sequence

It's not necessary to know how or when each function is called. I keep it here for documentation or in case someone wants to modify the code.
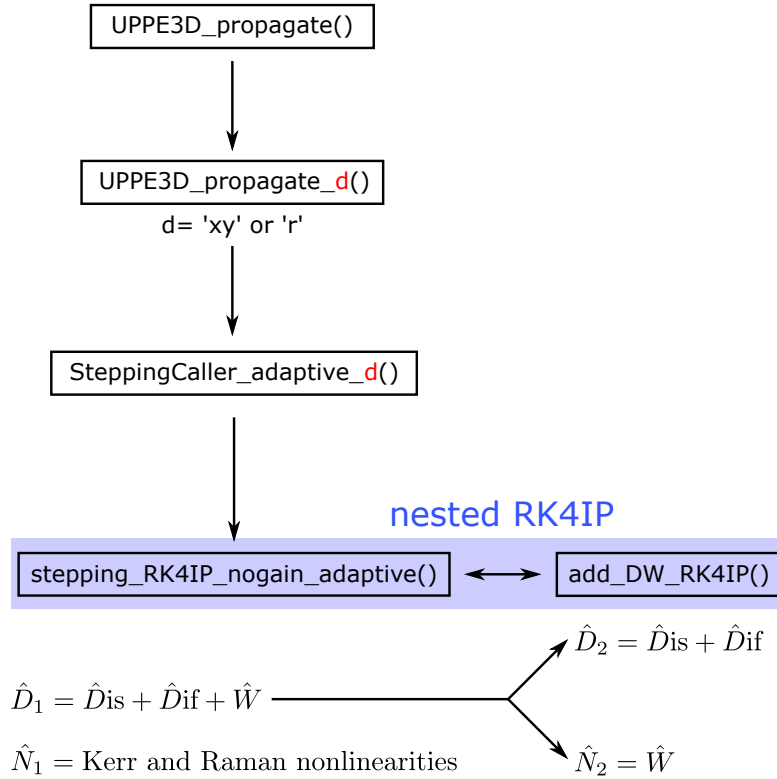

Figure 8.1: Diagram of the calling sequence.

The code uses "RK4IP" (Runge-Kutta in the interaction picture) [1, 2] with an adaptive step-size control, whose dispersion operation $\hat{D}_1$ contains dispersion $\hat{D}\mathrm{is}$, diffraction $\hat{D}\mathrm{if}$, and waveguide $\hat{W}$ effects, and nonlinear operation $\hat{N}_1$ contains Kerr and Raman nonlinearities. However, due to the incommutableness of the dispersion+diffraction $\hat{D}\mathrm{is} + \hat{D}\mathrm{if} \sim K_z$ and the waveguide $\hat{W} \sim k_W^2$ operators, we apply a second RK4IP for them whenever we need to apply $\hat{D}_1$. As typical dispersion and nonlinear operators that are incommutable, the nested RK4IP has a dispersion operator $\hat{D}_2 = \hat{D}\mathrm{is} + \hat{D}\mathrm{if}$ and a nonlinear operator $\hat{N}_2 = \hat{W}$. Because of two adaptive-step RK4IP, there are two threshold parameters to control each behavior, which by

default are both set to 10^{-6}.

Chapter 9

Derivation

In this chapter, I show the derivation of 3D-UPPE [Eq. (1.1)]. Although it has been shown in the paper [11], I realized that there are a few mistakes in equations. Filing an errata might be a future option, but it's good for me to have one document that I can easily edit and update.

In fiber optics, light propagates in a dielectric medium, or gas if it is a hollow-core fiber, with its waveguide boundary conditions. Since there are no charge and current sources, such electromagnetic fields are governed by the following Maxwell's equations:

$$\nabla \times \vec{\mathbb{E}}(\vec{x}, t) = -\mu_0 \partial_t \vec{\mathbb{H}}(\vec{x}, t) \tag{9.1a}$$

$$\nabla \times \vec{\mathbb{H}}(\vec{x}, t) = \epsilon_0 \partial_t \left[\epsilon_r(\vec{x}, t) * \vec{\mathbb{E}}(\vec{x}, t) \right] + \partial_t \vec{\mathbb{P}}(\vec{x}, t), \tag{9.1b}$$

where $\vec{\mathbb{E}}$ and $\vec{\mathbb{H}}$ are electric and magnetic fields, respectively; $\vec{\mathbb{P}}$ is the induced nonlinear polarization; ϵ_r is the relative dielectric constant of the medium; ϵ_0 and μ_0 are permittivity and permeability in vacuum. We can do spectral Fourier transform to the equations and consider only their positive-frequency components (analytic signal).

$$\mu_0 i\omega \vec{\mathcal{H}} = \nabla \times \vec{\mathcal{E}} \tag{9.2a}$$

$$\vec{\mathcal{J}} - i\omega \vec{\mathcal{P}} - i\omega \epsilon_0 \epsilon_r \vec{\mathcal{E}} = \nabla \times \vec{\mathcal{H}}, \tag{9.2b}$$

which leads to

$$\nabla \times \nabla \times \vec{\mathcal{E}} = \nabla \left(\nabla \cdot \vec{\mathcal{E}} \right) - \nabla^2 \vec{\mathcal{E}}$$
$$= \mu_0 i\omega \vec{\mathcal{J}} + \mu_0 \omega^2 \vec{\mathcal{P}} + \omega^2 \mu_0 \epsilon_0 \epsilon_r \vec{\mathcal{E}} \tag{9.3}$$

$\vec{\mathcal{E}}$, $\vec{\mathcal{H}}$, $\vec{\mathcal{J}}$, and $\vec{\mathcal{P}}$ are the complex-valued analytic signal of their corresponding real-valued counterparts. We assume that the electric field and the medium response (current $\vec{\mathcal{J}}$, nonlinear polarization $\vec{\mathcal{P}}$) are transverse, *i.e.*, perpendicular to the propagation direction determined by the wave number $\vec{k}$. This standard assumption in propagation of electromagnetic fields means that the term $\nabla \left(\nabla \cdot \vec{\mathcal{E}} \right)$ can be neglected. This remains valid as long as beams are not too strongly focused. When beam numerical aperture exceeds a few percent, a small longitudinal component $\vec{\mathcal{E}}$ may develop close to the focus and makes this approximation invalid. In addition, we also assume that there is no current $\vec{\mathcal{J}} = 0$. After these assumptions, we obtain

$$\nabla^2 \vec{\mathcal{E}}(\vec{r}_\perp, z, \omega) + k^2(\vec{r}_\perp, \omega) \vec{\mathcal{E}}(\vec{r}_\perp, z, \omega) = -\mu_0 \omega^2 \vec{\mathcal{P}}(\vec{r}_\perp, z, \omega), \tag{9.4}$$

where $k^2 = \omega^2 \mu_0 \epsilon_0 \epsilon_r$ and $\vec{r}_\perp = (x, y)$. Note that $\epsilon_r = \epsilon_r(\vec{r}_\perp, \omega)$ depends on x and y and is independent of z. This accounts for the variation in refractive index of the cross-sectional profile. We can split k^2 into its frequency-dependent part $k_\omega^2(\omega)$ and spatially-dependent (but frequency-independent) part $k_W^2(\vec{r}_\perp, \omega)$:

$$k^2(\vec{r}_\perp, \omega) = k_\omega^2(\omega) + k_W^2(\vec{r}_\perp, \omega). \qquad (9.5)$$

$k_W^2(\vec{r}_\perp, \omega)$ determines the waveguide effect. It is zero if the medium is homogeneous.

By transforming Eq. (9.4) into the cross-sectional $k_\perp$-space, we obtain

$$\left[\partial_z^2 + \left(k_\omega^2(\omega) - \left| \vec{k}_\perp \right|^2 \right) \right] \vec{\mathcal{E}}(\vec{k}_\perp, z, \omega) + \mathfrak{F}_{k_\perp} \left[k_W^2(\vec{r}_\perp, \omega) \vec{\mathcal{E}}(\vec{r}_\perp, z, \omega) \right] = -\mu_0 \omega^2 \vec{\mathcal{P}}(\vec{k}_\perp, z, \omega). \quad (9.6)$$

Its $\left[\partial_z^2 + \left(k_\omega^2(\omega) - \left| \vec{k}_\perp \right|^2 \right) \right]$ can be rewritten into $\left[\left(\partial_z + iK_z(\vec{k}_\perp, \omega) \right) \left(\partial_z - iK_z(\vec{k}_\perp, \omega) \right) \right]$, where $K_z(\vec{k}_\perp, \omega) = \sqrt{k_\omega^2(\omega) - \left| \vec{k}_\perp \right|^2}$. Assume that the forward propagating component is larger than the backward propagating one: $\partial_z \to iK_z$. The above equation becomes

$$\partial_z \vec{\mathcal{E}}(\vec{k}_\perp, z, \omega) = iK_z \vec{\mathcal{E}}(\vec{k}_\perp, z, \omega) + i\frac{1}{2K_z} \mathfrak{F}_{k_\perp} \left[k_W^2(\vec{r}_\perp, \omega) \vec{\mathcal{E}}(\vec{r}_\perp, z, \omega) \right] + i\frac{\omega^2}{2K_z c^2} \frac{\vec{\mathcal{P}}(\vec{k}_\perp, z, \omega)}{\epsilon_0}. \quad (9.7)$$

By introducing the envelope of the analytic signal:

$$\vec{\mathbb{E}}(\vec{x}, t) = \frac{1}{2} \left[\vec{\mathcal{E}}(\vec{x}, t) + \text{c.c.} \right] \quad , \vec{\mathcal{E}} \text{ is the analytic signal of } \vec{\mathbb{E}}$$

$$= \frac{1}{2} \left[\vec{E}(t) e^{i\left(\beta_{(0)} z - \omega_0 t \right)} + \text{c.c.} \right] \qquad (9.8a)$$

$$\vec{\mathbb{P}}(\vec{x}, t) = \frac{1}{2} \left[\vec{\mathcal{P}}(\vec{x}, t) + \text{c.c.} \right] \quad , \vec{\mathcal{P}} \text{ is the analytic signal of } \vec{\mathbb{P}}$$

$$= \frac{1}{2} \left[\vec{P}(t) e^{i\left(\beta_{(0)} z - \omega_0 t \right)} + \text{c.c.} \right], \qquad (9.8b)$$

Eq. (9.7) becomes

$$\partial_z \vec{E}(\vec{k}_\perp, z, \Omega) = i \left(K_z - \beta_{(0)} \right) \vec{E}(\vec{k}_\perp, z, \Omega) + i\frac{1}{2K_z} \mathfrak{F}_{k_\perp} \left[k_W^2(\vec{r}_\perp, \omega) \vec{E}(\vec{r}_\perp, z, \Omega) \right] + i\frac{\omega^2}{2K_z c^2} \frac{\vec{P}(\vec{k}_\perp, z, \Omega)}{\epsilon_0} \tag{9.9}$$

with the offset frequency $\Omega = \omega - \omega_0$ for the Fourier transform of $\vec{E}(t)$.

Kerr and Raman nonlinearity

Note that, in general, the nonlinear polarization has the following form [5]:

$$\vec{\mathbb{P}}(t) = \int_{-\infty}^{\infty} \chi^{(3)}(t_1, t_2, t_3) \vdots \vec{\mathbb{E}}(t - t_1) \vec{\mathbb{E}}(t - t_2) \vec{\mathbb{E}}(t - t_3) \, dt_1 \, dt_2 \, dt_3, \qquad (9.10)$$

where

$$\chi^{(3)}(t_1, t_2, t_3) = \delta(t_1)\delta(t_2 - t_3)\hat{R}^{ijk\ell}(t_3) \qquad (9.11a)$$

$$\hat{R}^{ijk\ell}(t) = \epsilon_0 \chi_{\text{electronic}}^{(3)} \frac{\delta^{ij}\delta^{k\ell} + \delta^{ik}\delta^{j\ell} + \delta^{i\ell}\delta^{jk}}{3} \delta(t) + \mathtt{R}_a(t)\delta^{ij}\delta^{k\ell} + \mathtt{R}_b(t)\frac{\delta^{ik}\delta^{j\ell} + \delta^{i\ell}\delta^{jk}}{2} \qquad (9.11b)$$

Cornell University

includes the instantaneous Kerr nonlinearity and the delayed isotropic (R_a) and anisotropic (R_b) Raman nonlinearities; therefore,

$$\mathbb{P}^i(t) = \sum_{jk\ell} \mathbb{E}^j(t) \int_{-\infty}^{\infty} \hat{R}^{ijk\ell}(\tau) \mathbb{E}^k(t-\tau) \mathbb{E}^\ell(t-\tau) \, \mathrm{d}\tau, \quad \text{by applying } (t_3 \to \tau). \tag{9.12}$$

First, we solve for the Kerr nonlinearity:

$$\mathbb{P}^i(\vec{r}, t) = \sum_{jkl} \epsilon_0 \frac{1}{2} \left[E^j(t) \mathrm{e}^{i(\beta_{(0)}z - \omega_0 t)} + \text{c.c.} \right] \chi_{\text{electronic}}^{(3)} \frac{\delta^{ij}\delta^{k\ell} + \delta^{ik}\delta^{j\ell} + \delta^{i\ell}\delta^{jk}}{3}$$

$$\times \frac{1}{2} \left[E^k(t) \mathrm{e}^{i(\beta_{(0)}z - \omega_0 t)} + \text{c.c.} \right] \frac{1}{2} \left[E^\ell(t) \mathrm{e}^{i(\beta_{(0)}z - \omega_0 t)} + \text{c.c.} \right]$$

$$= \frac{\epsilon_0 \chi_{\text{electronic}}^{(3)}}{8} \sum_k \left\{ \left(E^i(E^k)^2 \mathrm{e}^{3i(\beta_{(0)}z - \omega_0 t)} + \text{c.c.} \right) \right.$$

$$\left. + \left[\left((E^i)^*(E^k)^2 + 2E^i \left| E^k \right|^2 \right) \mathrm{e}^{i(\beta_{(0)}z - \omega_0 t)} + \text{c.c.} \right] \right\}. \tag{9.13}$$

Next, we solve for the isotropic Raman term:

$$\mathbb{P}^i(\vec{r}, t) = \frac{1}{2} \left[E^i(t) \mathrm{e}^{i(\beta_{(0)}z - \omega_0 t)} + \text{c.c.} \right] \int \mathsf{R}_a(\tau) \sum_k \left\{ \frac{1}{2} \left[E^k(t-\tau) \mathrm{e}^{i[\beta_{(0)}z - \omega_0(t-\tau)]} + \text{c.c.} \right] \right\}^2$$

$$= \frac{1}{8} \sum_k \left\{ \left[E^i(t) \mathrm{e}^{3i(\beta_{(0)}z - \omega_0 t)} \int \mathsf{R}_a(\tau) \left(E^k(t-\tau) \right)^2 \mathrm{e}^{2i\omega_0 \tau} \, \mathrm{d}\tau + \text{c.c.} \right] \right.$$

$$+ \left[2E^i(t) \mathrm{e}^{i(\beta_{(0)}z - \omega_0 t)} \int \mathsf{R}_a(\tau) \left| E^k(t-\tau) \right|^2 \mathrm{d}\tau + \text{c.c.} \right]$$

$$\left. + \left[\left(E^i(t) \right)^* \mathrm{e}^{i(\beta_{(0)}z - \omega_0 t)} \int \mathsf{R}_a(\tau) \left(E^k(t-\tau) \right)^2 \mathrm{e}^{2i\omega_0 \tau} \, \mathrm{d}\tau + \text{c.c.} \right] \right\}, \tag{9.14}$$

Cornell University

and the anisotropic term:

$$
\mathbb{P}^i(\vec{r}, t) = \sum_j \mathbb{E}^j(t) \int \mathsf{R}_b(\tau) \mathbb{E}^i(t-\tau) \mathbb{E}^j(t-\tau)\, d\tau
$$

$$
= \sum_j \frac{1}{2} \left[E^j(t) e^{i\left(\beta_{(0)}z - \omega_0 t\right)} + \text{c.c.} \right]
$$

$$
\int \mathsf{R}_b(\tau) \frac{1}{2} \left\{ E^i(t-\tau) e^{i\left[\beta_{(0)}z - \omega_0(t-\tau)\right]} + \text{c.c.} \right\} \frac{1}{2} \left\{ E^j(t-\tau) e^{i\left[\beta_{(0)}z - \omega_0(t-\tau)\right]} + \text{c.c.} \right\} d\tau
$$

$$
= \frac{1}{8} \sum_j \left\{ \left[E^j(t) e^{3i\left(\beta_{(0)}z - \omega_0 t\right)} \int \mathsf{R}_b(\tau) E^i(t-\tau) E^j(t-\tau) e^{2i\omega_0\tau} + \text{c.c.} \right] \right.
$$

$$
+ \left[E^j(t) e^{i\left(\beta_{(0)}z - \omega_0 t\right)} \int \mathsf{R}_b(\tau) \left(E^i(E^j)^* + (E^i)^* E^j \right)(t-\tau)\, d\tau + \text{c.c.} \right]
$$

$$
\left. + \left[(E^j)^* e^{i\left(\beta_{(0)}z - \omega_0 t\right)} \int \mathsf{R}_b(\tau) E^i(t-\tau) E^j(t-\tau) e^{2i\omega_0\tau}\, d\tau + \text{c.c.} \right] \right\}.
$$

$$(9.15)$$

By ignoring the 3rd harmonic terms, which are terms with $e^{3i\left(\beta_{(0)}z - \omega_0 t\right)}$, the polarization can be expressed, in terms of its envelope, as

$$
P^i(\vec{r}, t) = \frac{1}{4} \sum_j \left\{ \epsilon_0 \chi^{(3)}_{\text{electronic}} \left[(E^i)^* (E^j)^2 + 2E^i \left| E^j \right|^2 \right] \right.
$$

$$
+ 2E^i(t) \int \mathsf{R}_a(\tau) \left| E^j(t-\tau) \right|^2 d\tau + (E^i)^*(t) \int \mathsf{R}_a(\tau)(E^j)^2(t-\tau) e^{2i\omega_0\tau}\, d\tau
$$

$$
+ E^j(t) \int \mathsf{R}_b(\tau) \left(E^i(E^j)^* + (E^i)^* E^j \right)(t-\tau)\, d\tau
$$

$$
\left. + (E^j(t))^* \int \mathsf{R}_b(\tau) \left(E^i E^j \right)(t-\tau) e^{2i\omega_0\tau}\, d\tau \right\}.
$$

$$(9.16)$$

We further ignore the delay terms, and obtain

$$
P^i(\vec{r}, t) = \frac{1}{4} \sum_j \left\{ \epsilon_0 \chi^{(3)}_{\text{electronic}} \left[(E^i)^* (E^j)^2 + 2E^i \left| E^j \right|^2 \right] \right.
$$

$$
+ 2E^i(t) \int \mathsf{R}_a(\tau) \left| E^j(t-\tau) \right|^2 d\tau
$$

$$
\left. + E^j(t) \int \mathsf{R}_b(\tau) \left(E^i(E^j)^* + (E^i)^* E^j \right)(t-\tau)\, d\tau \right\}.
$$

$$(9.17)$$

Since $\vec{E}$ above has the unit of V/m, we transform it into $\sqrt{\text{W/m}^2}$, a more commonly used physical quantity such that $\left| \vec{\mathbb{A}} \right|^2$ directly corresponds to the intensity (in W/m^2). The transformation relies on $\left| \vec{\mathbb{A}} \right|^2 = \frac{\epsilon_0 n_{\text{eff}} c}{2} \left| \vec{E} \right|^2$, where $\vec{\mathbb{A}}$ has a unit of $\sqrt{\text{W/m}^2}$. The transformed

equation looks the same as Eq. (9.9) by replacing $\vec{E}$ with $\vec{\mathbb{A}}$, but the nonlinear polarization $\vec{P}$ becomes

$$(P')^i(\vec{r}, t) = \sqrt{\frac{\epsilon_0 n_{\text{eff}} c}{2}} P^i(\vec{r}, t) = \frac{1}{2\epsilon_0 n_{\text{eff}} c} \sum_j \left\{ \epsilon_0 \chi^{(3)}_{\text{electronic}} \left[(\mathbb{A}^i)^*(\mathbb{A}^j)^2 + 2\mathbb{A}^i \left| \mathbb{A}^j \right|^2 \right] \right.$$
$$+ 2\mathbb{A}^i(t) \int R_a(\tau) \left| \mathbb{A}^j(t-\tau) \right|^2 d\tau$$
$$\left. + \mathbb{A}^j(t) \int R_b(\tau) \left(\mathbb{A}^i(\mathbb{A}^j)^* + (\mathbb{A}^i)^*\mathbb{A}^j \right)(t-\tau) d\tau \right\}.$$
$$(9.18)$$

Consider the moving frame:

$$T = t - \beta_{(1)} z \quad \Rightarrow \quad \partial_z \mathbb{A}(\vec{r}, t) = \partial_z \mathbb{A}(\vec{r}, T) - \beta_{(1)} \partial_T \mathbb{A}(\vec{r}, T), \tag{9.19}$$

where the ∂_z on the left-hand side is actually a total derivative.

$$\partial_z \vec{\mathbb{A}}(\vec{k}_\perp, z, \Omega) = i \left[K_z - \left(\beta_{(0)} + \beta_{(1)}\Omega \right) \right] \vec{\mathbb{A}}(\vec{k}_\perp, z, \Omega) + i \frac{1}{2K_z} \mathfrak{F}_{k_\perp} \left[k_W^2(\vec{r}_\perp, \omega) \vec{\mathbb{A}}(\vec{r}_\perp, z, \Omega) \right]$$
$$+ i \frac{\omega^2}{2K_z c^2} \frac{\vec{P}'(\vec{k}_\perp, z, \Omega)}{\epsilon_0}. \tag{9.20}$$

If we apply the model commonly used in solid-core silica fiber, where

$$\epsilon_0 \chi^{(3)}_{\text{electronic}} = (1 - f_R)\, \epsilon_0 \chi^{(3)}_{xxxx} = (1 - f_R) \frac{4\epsilon_0^2 n_{\text{eff}}^2 c}{3} n_2 \tag{9.21a}$$

$$R_a = f_R f_a \epsilon_0 \chi^{(3)}_{xxxx} \frac{3}{2} h_a = 2 f_R f_a \epsilon_0^2 n_{\text{eff}}^2 c n_2 h_a(t) \tag{9.21b}$$

$$R_b = f_R f_b \epsilon_0 \chi^{(3)}_{xxxx} \frac{3}{2} h_b = 2 f_R f_b \epsilon_0^2 n_{\text{eff}}^2 c n_2 h_b(t), \tag{9.21c}$$

we obtain Eq. (1.3). On the other hand, gas's Raman response is directly derived with R_a and R_b in $\frac{1}{2} R_a(t) = R_a(t)$ and $\frac{1}{2} R_b(t) = R_b(t)$ [6], so we can easily obtain Eq. (1.5).

In our derivation of nonlinearities, we assume that the electronic nonlinear coefficient $\chi^{(3)}_{\text{electronic}}$ and the effective index n_{eff} are constants. Their frequency dependence is artificially recovered later after the spectral Fourier transform [Eqs. (1.3) and (1.5)], which seems not justifiable *a priori* but has been shown to improve the result [12–14].

Because K_z can be close to 0 as $|k_\perp|^2$ is huge, which can easily happen under a decently-huge $k_\perp$-space (with fine spatial sampling), the computation of the nonlinear term will easily blow up due to the $1/K_z$ term, artificially producing unreasonable results. Therefore, to simplify the simulation process, K_z in the denominator of the nonlinear term is replaced with k_ω. This assumption fails when the light has high-$\vec{k}_\perp$ components, such as tightly-focusing. However, during the derivation, we have already assumed that all the field and the responses are transverse to make $\nabla \left(\nabla \cdot \vec{\mathcal{E}} \right) = 0$, so the assumption for $K_z \to k_\omega$ makes sense. For potentially higher

Cornell University

accuracy, this replacement can be applied with

$$\frac{1}{K_z} = \frac{1}{\sqrt{k_\omega^2(\omega) - \left|\vec{k}_\perp\right|^2}} = \frac{1}{k_\omega\sqrt{1 - \frac{|\vec{k}_\perp|^2}{k_\omega^2}}}$$

$$\approx \frac{1}{k_\omega}\left(1 + \frac{\left|\vec{k}_\perp\right|^2}{2k_\omega^2}\right). \tag{9.22}$$

Eq. (9.22) approximates $\frac{1}{K_z}$ well as $\left|\vec{k}_\perp\right| \ll k_\omega$. Although it induces deviation at large $\left|\vec{k}_\perp\right|$, it does not blow up to infinity as the original $\frac{1}{K_z}$ but rather only slowly increases (such as approaching 1.5 as $\left|\vec{k}_\perp\right| \to k_\omega$). As a result, the replacement with Eq. (9.22) not only introduces more accuracy but is also numerically stable. After all, we achieve deriving the final 3D-UPPE in Eq. (1.1).

Cornell University

Chapter 10

Photoionization

In this section, we include the photoionization effect in the pulse propagation equation and generalize the UPPE in the supplement of [15]. When the pulse becomes strong, it is likely to *ionize* the gas, inducing special effects, such as photoionization-induced blueshift [16, 17]. It is important to take this effect into account in simulations, especially for strong pulses. In our cases, we use pulse energies up to multi-millijoule; it then raises the question of whether ionization takes place, despite the strong frequency chirping to 10 ps.

There are several papers that discuss the photoionization effect. However, some of them do not include all the details, for example, leaving the most important ionization rate $W(t)$ in references [18–20]. In addition, most of them rely on the *real-valued* electric field $\vec{\mathbb{E}}$ [21–23], instead of the *analytic-signal* $A(t)$ [24, 25] commonly used in the laser field. It is also easier to solve with *analytic signal* because only the frequency window around the pulse is required; however, with a real-valued field $\vec{\mathbb{E}}$, the frequency window spans a wide range from negative frequencies to positive ones, whose simulation thus becomes computationally heavy. Most importantly, most previous work on gas-based nonlinear optics in hollow-core fibers are based on the Ammosov–Delone–Krainov (ADK) model due to its simple implementation [18, 20, 22, 23]; however, the ADK model works the best only when the Keldysh parameter $\gamma < 1/2$ which is satisfied only by strong low-frequency fields. Here, we intend to implement the Perelomov-Popov-Terent'ev (PPT) model, which works for an arbitrary Keldysh parameter [26]. It is an appropriate model for us, since our pulses have Keldysh parameters larger than 1. Besides, in this section, we will demonstrate its feasibility with a Keldysh parameter around 1 when photoionization-induced blueshift takes place, which is also used to verify our model. In addition to representations with atomic units commonly used in studies of atomic physics, we transform them into the SI unit to accommodate for the laser fields and the implementation into UPPE. The introduction follows Hussien's thesis, which has by far been the best one I've read [27], followed by our integration of photoionization into the UPPE.

10.1 Keldysh parameter

When an electric field is applied to an atomic potential, it will interact with the potential, inducing various types of photoionization (Fig. 10.1). If the oscillating electric field has a low frequency and high intensity, it distorts the potential. The electron in the potential well is able to escape through either tunneling under a decent distortion [Fig. 10.1(c)] or direct evolution into an unbounded ground state under an enormously strong field [Fig. 10.1(d)]. If the field, on

the other side of the spectrum, has a high frequency and relatively low intensity, multiphoton process dominates such that an electron escapes by absorbing multiple photons [Fig. 10.1(b)]. The N-photon ionization rate is, intuitively, proportional to $\left[I/(\hbar\omega) \right]^N$. The simplest example is the *photoelectric effect* through single-photon absorption explained by Einstein in 1905 [28].
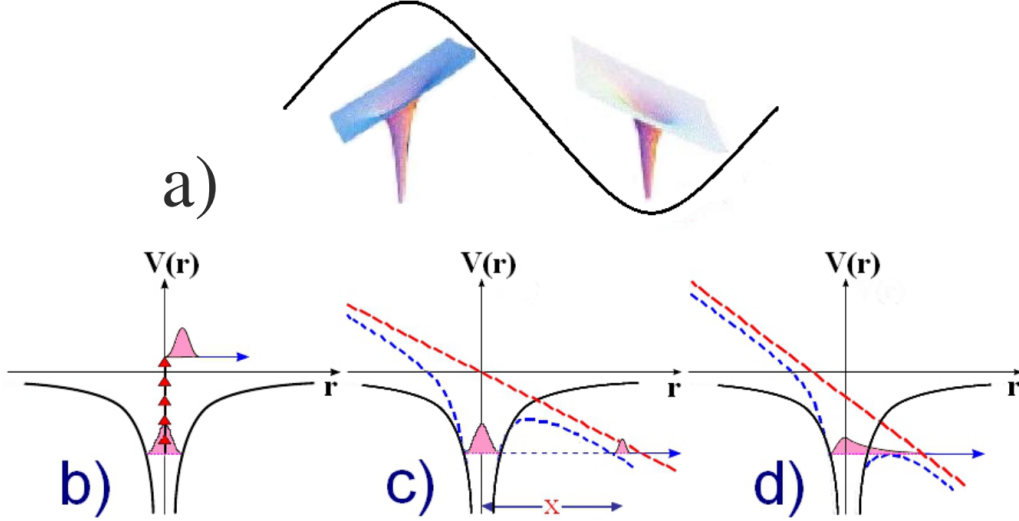

Figure 10.1: Figure 2.2 in [27]. Below is quoted from the figure of Hussien's thesis: "Schematic diagram in which the electric field is shown as oscillating field, which tilts the atomic potential (a) and the three main ionization mechanisms in the nonlinear regime: (b) multi-photon ionization, (c) tunneling ionization and (d) over-the-barrier ionization. The black curves represent the original (field-free) Coulomb potential and the dashed blue curves represent the distorted Coulomb potential by the external field, while the sloped long-dashed line is the laser field potential. The dotted magenta lines show the energy of the least bound electron in the field-free case. The tunneling path is indicated by the red dashed line."

Among studies of ionization, *Keldysh parameter* is a dimensionless metric to determine the regime the system is in, multiphoton absorption or "tunneling and over-the-barrier ionization". It is defined as the ease/difficulty for an electron to tunnel through a potential barrier:

$$\gamma \sim \frac{t_{\text{tunneling}}}{\frac{1}{2}t_{\text{laser cycle}}} \sim \frac{\text{tunneling width/tunneling velocity}}{\frac{1}{2}t_{\text{laser cycle}}} = \frac{\left(\frac{E_b}{e\left|\vec{\mathbb{E}}\right|} \right) / \sqrt{\frac{2E_b}{m_e}}}{\pi/\omega} = \frac{\omega\sqrt{2m_e E_b}}{2\pi e\left|\vec{\mathbb{E}}\right|}$$

$$\Rightarrow \gamma = \frac{\omega\sqrt{2m_e E_b}}{e\left|\vec{\mathbb{E}}\right|} = \sqrt{\frac{E_b}{2U_p}}, \tag{10.1}$$

where E_b is the ionization energy in the Coulomb potential, $e = 1.602\,176\,63 \times 10^{-19}\,\text{C}$ is the electron charge, $m_e = 9.109\,383\,7 \times 10^{-31}\,\text{kg}$ is the electron mass (in silica, it becomes $0.64m_e$ [29]), $\left|\vec{\mathbb{E}}\right|$ is the strength of the electric field (V/m), and ω is the field angular frequency (rad), U_p is the ponderomotive energy (J) with

$$U_p = \frac{e^2 F^2}{4m_e\omega^2}, \tag{10.2}$$

in which $U_p(\text{eV}) \approx 9.33 \times 10^{-14} I(\text{W/cm}^2) \lambda^2(\mu\text{m})$ is commonly used to calculate ponderomotive energy in electronvolts. The notation used here is to conform with those in atomic physics, as well as Hussien's thesis.

10.2 Photoionization models

In this section, I'll introduce two common photoionization models: the Ammosov–Delone–Krainov (ADK) model and the Perelomov-Popov-Terent'ev (PPT) model. The ADK model is applicable only in the small-Kelysh-parameter regime ($\gamma < 1$) while the PPT model works for an arbitrary *gamma*.

10.2.1 Ammosov–Delone–Krainov (ADK) model for tunneling ionization

Strong fields with a low frequency can ionize atoms efficiently and directly without involving intermediate states as in multiphoton ionization. Experiments have shown that tunneling can happen when $\gamma < 1/2$ [30].

To begin with, we start with the ionization rate of a hydrogen atom under a static electric field. Note that the notations here are given in the atomic units. Perelomov *et al.* have shown that [26]

$$W_{\text{static}}^{\text{ADK}} = \sum_m \left|C_{n,\ell}\right|^2 f(\ell, m) E_b \left(\frac{2F_0}{F}\right)^{2n-|m|-1} e^{-\frac{2F_0}{3F}}, \tag{10.3}$$

where F is the electric field, $F_0 = (2E_b)^{3/2}$, $\left(2F_0/F\right)^{2n}$ corresponds to the long-range effect of a Coulomb potential, $C_{n,\ell}$ and $f(\ell, m)$ contain information about the initial atomic state with

$$\left|C_{n,\ell}\right|^2 = \frac{2^{2n}}{n(n+\ell)!(n-\ell-1)!} \tag{10.4a}$$

$$f(\ell, m) = \frac{(2\ell+1)(\ell+|m|)!}{2^{|m|}|m|!(\ell-|m|!)!} \tag{10.4b}$$

To use this equation beyond hydrogen, Ammosov, Delone, and Krainov have extended it with the following substitute of parameters:

$$n \to n^* = Z\left(2E_b\right)^{-1/2} \tag{10.5a}$$

$$\ell \to \ell^* = \begin{cases} 0 & , \ell \ll n^* - 1 \\ n^* - 1 & , \text{otherwise} \end{cases}, \tag{10.5b}$$

where Z is the multiplicity of the atom or molecule.

The formula becomes different with an alternating field such that

$$\vec{F}(t) = F\cos(\omega t)\hat{e}_x. \tag{10.6}$$

Because $1/\cos(\omega t) \approx 1 + (\omega t)^2/2$ and the exponential dependence shows a dominant contribution only around $\omega t \to 0$, the instantaneous ionization rate is, from Eq. (10.3),

$$W_{\text{instantaneous}} = W_{\text{static}} e^{-\frac{F_0}{3F}(\omega t)^2} \tag{10.7}$$

Cornell University

Assume that the field is oscillating much faster than the electron tunneling time such that it follows the envelope of the field adiabatically. This leads to the *cycle-averaged* ionization rate

$$W_{\text{AC}} = \frac{1}{\pi} \int_{-\frac{\pi}{2}}^{\frac{\pi}{2}} W_{\text{instantaneous}}(t)\, \mathrm{d}(\omega t) \approx \frac{W_{\text{static}}}{\pi} \sqrt{\frac{3F}{F_0}} \int_{-\infty}^{\infty} \mathrm{e}^{-x^2}\, \mathrm{d}x = \sqrt{\frac{3F}{\pi F_0}} W_{\text{static}} \qquad (10.8)$$

10.2.2 Perelomov-Popov-Terent'ev (PPT) model for an arbitrary Keldysh parameter

Despite the simplicity of the ADK model, its feasibility is limited to small γ. To calculate the ionization rate for an arbitrary Keldysh parameter γ, it is important to apply the PPT model that goes beyond the limit of static fields and into the high-frequency regime where multiphoton ionization dominates [26]. The result is shown below:

$$W_{\text{AC}}^{\text{PPT}} = \sum_m \left|C_{n^*,\ell^*}\right|^2 f(\ell, m) E_b \sqrt{\frac{6}{\pi}} \left(\frac{2F_0}{F\sqrt{1+\gamma^2}}\right)^{2n-|m|-3/2} A_m(\omega, \gamma) \mathrm{e}^{-\frac{2F_0}{3F} g(\gamma)}, \qquad (10.9)$$

with

$$A_m(\omega, \gamma) = \frac{4}{\sqrt{3\pi}} \frac{1}{|m|!} \frac{\gamma^2}{1+\gamma^2} \sum_{\tilde{n}>\nu}^{\infty} \left[\mathrm{e}^{-\alpha(\tilde{n}-\nu)} B_m\left(\sqrt{\beta(\tilde{n}-\nu)}\right)\right] \qquad (10.10\text{a})$$

$$B_m(x) = \frac{x^{2|m|+1}}{2} \int_0^1 \frac{\mathrm{e}^{-x^2 t} t^{|m|}}{\sqrt{1-t}}\, \mathrm{d}t \qquad (10.10\text{b})$$

$$\alpha(\gamma) = 2\left(\sinh^{-1}\gamma - \frac{\gamma}{\sqrt{1+\gamma^2}}\right) \qquad (10.10\text{c})$$

$$\beta(\gamma) = \frac{2\gamma}{\sqrt{1+\gamma^2}} \qquad (10.10\text{d})$$

$$g(\gamma) = \frac{3}{2\gamma}\left[\left(1+\frac{1}{2\gamma^2}\right)\sinh^{-1}\gamma - \frac{\sqrt{1+\gamma^2}}{2\gamma}\right] \approx \begin{cases} 1 - \frac{1}{10}\gamma^2 + \frac{9}{280}\gamma^4 & , \gamma \ll 1 \\ \frac{3}{2\gamma}\left[\ln(2\gamma) - \frac{1}{2}\right] & , \gamma \gg 1 \end{cases} \qquad (10.10\text{e})$$

$$\tilde{n} = \lfloor \frac{E_b}{\omega} + 1 \rfloor + S \quad , S = 0, 1, 2, \ldots \qquad (10.10\text{f})$$

$$\nu = \frac{E_b}{\omega}\left(1 + \frac{1}{2\gamma^2}\right), \qquad (10.10\text{g})$$

where the summation in A_m sums over S, and $\lfloor \cdot \rfloor$ finds its integer part. When $\gamma \to 0$, all terms in the summation contribute equally. Summation is then transformed into an integral and leads to $A_m \approx 1$ which further reduces to the AC version of Eq. (10.3). On the contrary, when $\gamma \gg 1$, only the first few terms in A_m contribute the most. Note that $\sinh^{-1}\gamma$ is the *arcsinh* function, rather than $1/\sinh\gamma$.

10.3 Integration into the UPPE for gases

Despite the higher accuracy of the PPT model over various Keldysh parameters, most people still prefer the ADK model due to its simplicity. The complexity results from the calculation of

Cornell University

the A_m factor. To implement it in our model, especially when $\gamma > 1$, it is important to further simplify this formula.

10.3.1 Ionization rates

If $F_0/F \gg 1$, from Eq. (10.9), the ionization rate is the largest when $m = 0$. Here, we consider only the ionization of electrons in the "s" and "p" states.

"s" state

In the "s" state, such as hydrogen and helium, $n^* = (2E_b)^{-1/2}$ and $\ell^* = 0$ [Eq. (10.5)]. In addition, $m = 0$, too.

$$
\begin{aligned}
B_0(x) &= \frac{x}{2} \int_0^1 \frac{e^{-x^2 t}}{\sqrt{1-t}} \, dt \\
&= x \int_0^{\pi/2} e^{-x^2 \sin^2 \theta} \sin \theta \, d\theta \quad , \text{let } t = \sin^2 \theta \\
&= x \int_0^{\pi/2} e^{-x^2 + x^2 \cos^2 \theta} \sin \theta \, d\theta \\
&= e^{-x^2} \int_0^x e^{u^2} \, du \quad , \text{let } u = x \cos \theta \\
&= -i e^{-x^2} \int_0^{ix} e^{-v^2} \, dv \quad , \text{let } v = iu \\
&= -i e^{-x^2} \frac{\sqrt{\pi}}{2} \operatorname{erf}(ix) \\
&= e^{-x^2} \frac{\sqrt{\pi}}{2} \operatorname{erfi}(x),
\end{aligned}
\tag{10.11}
$$

where $\operatorname{erf}(\cdot)$ is the error function and $\operatorname{erfi}(\cdot)$ is the imaginary error function. They are related by $\operatorname{erfi}(x) = -i \operatorname{erf}(ix)$. With this relation, we can simplify A_m as

$$
\begin{aligned}
A_0(\omega, \gamma) &= \frac{4}{\sqrt{3\pi}} \frac{\gamma^2}{1+\gamma^2} \sum_{S=0}^{\infty} e^{\alpha(\tilde{n}-\nu)_S} e^{-\beta(\tilde{n}-\nu)_S} \frac{\sqrt{\pi}}{2} \operatorname{erfi}(\sqrt{\beta(\tilde{n}-\nu)_S}) \\
&= \frac{2}{\sqrt{3}} \frac{\gamma^2}{1+\gamma^2} \sum_{S=0}^{\infty} e^{-(\alpha+\beta)(\tilde{n}-\nu)_S} \operatorname{erfi}(\sqrt{\beta(\tilde{n}-\nu)_S}) \\
&= \frac{2}{\sqrt{3}} \frac{\gamma^2}{1+\gamma^2} \sum_{S=0}^{\infty} e^{-2\left(\sinh^{-1} \gamma\right)(\tilde{n}-\nu)_S} \operatorname{erfi}(\sqrt{\beta(\tilde{n}-\nu)_S})
\end{aligned}
\tag{10.12}
$$

Next, we solve for $(\tilde{n} - \nu)_S$.

$$
\begin{aligned}
(\tilde{n} - \nu)_S &= \lfloor \frac{E_b}{\omega} + 1 \rfloor + S' - \frac{E_b}{\omega}\left(1 + \frac{1}{2\gamma^2}\right) > 0 \\
&= \lceil \nu \rceil - \nu + S \quad , S = 0, 1, 2, \dots
\end{aligned}
\tag{10.13}
$$

where $\lceil \cdot \rceil$ is the ceiling function. In practice, it is not possible to sum over an infinite number of terms. Fig. 10.2 shows the shape of A_0 with different numbers of summations. The leading

Cornell University

term, $S = 0$, approximates A_0 pretty well when the Keldysh parameter $\gamma > 3$. However, it decreases when $\gamma \to 0$. In this regime, each term in the summation becomes smaller and contributes equally to A_0, so considering only the first term is insufficient. By summing 11 terms ($S = 0 \sim 10$), it can approximate A_0 well down to $\gamma = 0.8$. If $\gamma < 0.8$, we artificially set $A_0 = 1$.
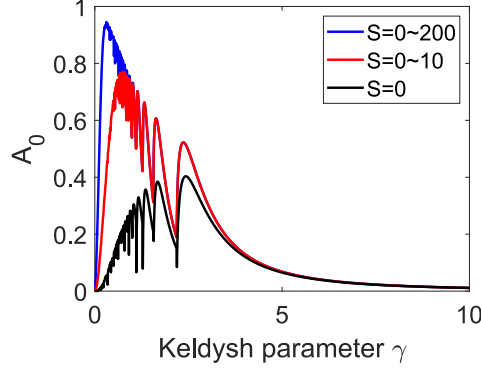

Figure 10.2: $A_0(\gamma)$ with different numbers of summation terms under an 0.8-µm electric field. $S = 0 \sim m$ means that it is summed over $S = 0$ to $S = m$ in Eq. (10.12).

Interestingly, there are oscillations in A_0. With a fixed field intensity, these oscillations represent the absorption of different numbers of photons of different frequencies, a feature of multiphoton ionization. Varying intensity has an effect similar to varying frequency in A_0, so, in Fig. 10.2, each peak represents the intensity that maximizes the absorption of each N-photons.

With A_0, we're ready to solve for ionization rate equation [Eq. (10.9)]. Since the "s" state has $n^* = (2E_b)^{-1/2}$, $m = 0$, and $\ell^* = 0$, Eq. (10.9) for the "s" state can be simplified to

$$W_{\text{AC}}^{\text{PPT}}\bigg|_{\text{"s" state}} \approx \frac{2^{2n^*}}{n^* \Gamma(n^* + 1)\Gamma(n^*)} E_b \sqrt{\frac{6}{\pi}} \left(\frac{2F_0}{F\sqrt{1+\gamma^2}}\right)^{2n^*-3/2} A_0(\omega, \gamma) e^{-\frac{2F_0}{3F}g(\gamma)}, \quad (10.14)$$

where the factorial is replaced by $\Gamma(n) = (n-1)!$, the Gamma function, in case that n^* is not an integer.

"p" state

For other inert gases whose highest occupied state is "p" state ($\ell = 1$), $m = 0$ should still dominate $W_{\text{AC}}^{\text{PPT}}$ as long as $F_0/F \gg 1$. Here, I solve for B_1, which is used in calculating A_1. To more accurately consider the ionization of inert gases or molecules beyond hydrogen and helium, it is added to the overall ionization rate.

$$\begin{aligned}
B_{\pm 1}(x) &= \frac{x^3}{2} \int_0^1 \frac{e^{-x^2 t} t}{\sqrt{1-t}} \, \mathrm{d}t \\
&= x^3 \int_0^{\pi/2} e^{-x^2 \sin^2 \theta} \sin^3 \theta \, \mathrm{d}\theta \quad , \text{let } t = \sin^2 \theta \\
&= x^3 \int_0^{\pi/2} e^{-x^2 + x^2 \cos^2 \theta} \sin^3 \theta \, \mathrm{d}\theta
\end{aligned}$$

$$= \int_0^x e^{u^2 - x^2} \left(x^2 - u^2 \right) du \quad , \text{let } u = x \cos\theta$$

$$= e^{-x^2} \left(x^2 \int_0^x e^{u^2} du - \int_0^x u^2 e^{u^2} du \right) \tag{10.15}$$

Let's digress for a while and calculate the following:

$$\int_0^x e^{t^2 u^2} du = \int_0^{ixt} e^{-v^2} \left(\frac{-i}{t} \right) dv \quad , \text{let } v = itu$$

$$= \frac{-i}{t} \frac{\sqrt{\pi}}{2} \operatorname{erf}(ixt)$$

$$= \frac{\sqrt{\pi}}{2t} \operatorname{erfi}(xt). \tag{10.16}$$

With $s = t^2$, it becomes

$$\int_0^x e^{su^2} du = \frac{\sqrt{\pi}}{2\sqrt{s}} \operatorname{erfi}(x\sqrt{s}). \tag{10.17}$$

By knowing that $\frac{d}{dz} \operatorname{erfi} z = \frac{2}{\sqrt{\pi}} e^{z^2}$, we can take the derivative of Eq. (10.17) with respect to s and obtain

$$\int_0^x u^2 e^{su^2} du = -\frac{\sqrt{\pi}}{4s^{1.5}} \operatorname{erfi}(x\sqrt{s}) + \frac{x}{2s} e^{x^2 s}. \tag{10.18}$$

Let $s = 1$, we get

$$\int_0^x u^2 e^{u^2} du = -\frac{\sqrt{\pi}}{4} \operatorname{erfi}(x) + \frac{x}{2} e^{x^2}. \tag{10.19}$$

From Eq. (10.11), we know $\int_0^x e^{u^2} du = \frac{\sqrt{\pi}}{2} \operatorname{erfi}(x)$. Therefore, we obtain

$$B_{\pm 1}(x) = e^{-x^2} \left[\frac{\sqrt{\pi}}{2} x^2 \operatorname{erfi}(x) + \frac{\sqrt{\pi}}{4} \operatorname{erfi}(x) - \frac{x}{2} e^{x^2} \right], \tag{10.20}$$

which gives

$$A_{\pm 1}(\omega, \gamma) = \frac{4}{\sqrt{3\pi}} \frac{\gamma^2}{1 + \gamma^2} \sum_{S=0}^{\infty} \left[e^{-\alpha(\tilde{n} - \nu)} B_m \left(\sqrt{\beta(\tilde{n} - \nu)} \right) \right]$$

$$= \frac{4}{\sqrt{3\pi}} \frac{\gamma^2}{1 + \gamma^2} \sum_{S=0}^{\infty} \left\{ e^{-2\left(\sinh^{-1} \gamma \right)(\tilde{n} - \nu)S} \right.$$

$$\left. \times \left\{ \frac{\sqrt{\pi}}{2} \left[\beta(\tilde{n} - \nu) \right] \operatorname{erfi}(\sqrt{\beta(\tilde{n} - \nu)}) + \frac{\sqrt{\pi}}{4} \operatorname{erfi}(\sqrt{\beta(\tilde{n} - \nu)}) - \frac{\sqrt{\beta(\tilde{n} - \nu)}}{2} e^{\beta(\tilde{n} - \nu)} \right\} \right\} \tag{10.21}$$

With $A_{\pm 1}$, we can then easily sum over all $m = -1, 0, 1$ to find the total ionization rate $W_{\text{AC}}^{\text{PPT}}$ for the "p" state:

$$W_{\text{AC}}^{\text{PPT}} \bigg|_{\text{"p" state}} \approx \sum_{m=-1}^{1} |C_{n,\ell}|^2 f(\ell, m) E_b \sqrt{\frac{6}{\pi}} \left(\frac{2F_0}{F\sqrt{1 + \gamma^2}} \right)^{2n^* - |m| - 3/2} A_m(\omega, \gamma) e^{-\frac{2F_0}{3F} g(\gamma)}, \tag{10.22}$$

Cornell University

For higher-order terms like B_2, B_3, etc., the same technique should also be applicable to solve for their analytic forms.

Conclude with both states

We have now finished deriving the ionization rate $W_{\text{AC}}^{\text{PPT}}$ required in our model. To implement it, we transform it from the previous atomic unit into the SI unit. In the atomic-unit system, each parameter is normalized such that they are unitless, so to transform them into the SI unit, we need the following relations:

$$\text{rate: } W^{a.u.} = \frac{W^{SI}}{e^2/(a_0 k\hbar)} = \frac{W^{SI}}{2E_{b,\text{H}}/\hbar} \tag{10.23a}$$

$$\text{frequency: } \omega^{a.u.} = \frac{\omega^{SI}}{e^2/(a_0 k\hbar)} = \frac{\omega^{SI}}{2E_{b,\text{H}}/\hbar} \tag{10.23b}$$

$$\text{ionization energy: } E_b^{a.u.} = \frac{E_b^{SI}}{e^2/(ka_0)} = \frac{E_b^{SI}}{2E_{b,\text{H}}} \tag{10.23c}$$

$$\text{electric field: } F^{a.u.} = \frac{F^{SI}}{e/(ka_0^2)} = \frac{F^{SI}}{2E_{b,\text{H}}/(a_0 e)}, \tag{10.23d}$$

where $a_0 = k\hbar^2/(m_e e^2)$ is the Bohr radius, $k = 4\pi\epsilon_0$, and $E_{b,\text{H}} = e^2/(2ka_0) = 13.6\,\text{eV}$ is the ionization energy of a hydrogen atom. We then obtain the ionization rate in the SI unit:

$$W_{\text{AC}}^{\text{PPT}} \approx \sum_m \left|C_{n^*,\ell^*}\right|^2 f(\ell,m) \frac{E_b}{\hbar} \sqrt{\frac{6}{\pi}} \left(\frac{\kappa}{\left|\vec{\mathbb{E}}\right|\sqrt{1+\gamma^2}}\right)^{2n^*-|m|-3/2} A_m(\omega,\gamma)\text{e}^{-\frac{\kappa}{3|\vec{\mathbb{E}}|}g(\gamma)}, \tag{10.24}$$

where $n^* = Z\sqrt{E_{b,\text{H}}/E_b}$, $\kappa = 4E_b\sqrt{2m_e E_b}/(\hbar e)$, and $\vec{\mathbb{E}}$ is the real-valued electric field. We ignore the "SI" superscript for simplicity, but the equation above uses all parameters in the SI unit.

Note that we also need to transform ν to calculate $(\tilde{n} - \nu)_S$ in the SI unit, which is shown below:

$$\nu = \frac{E_b}{\hbar\omega}\left(1 + \frac{1}{2\gamma^2}\right). \tag{10.25}$$

The photoionization-induced polarization is governed by [21]

$$\frac{\partial\left|\vec{\mathbb{P}}_I\right|}{\partial t} = \frac{e^2}{m_e}\int_{-\infty}^t \rho_e(t')\left|\vec{\mathbb{E}}(t')\right|\text{d}t' + \frac{\partial\rho_e}{\partial t}\frac{E_b}{\left|\vec{\mathbb{E}}(t)\right|}$$

$$= \frac{e^2}{m_e}\int_{-\infty}^t \rho_e(t')\left|\vec{\mathbb{E}}(t')\right|\text{d}t' + \frac{\partial\rho_e}{\partial t}\frac{E_b}{\left|\vec{\mathbb{E}}(t)\right|^2}\left|\vec{\mathbb{E}}(t)\right| \tag{10.26}$$

where $\vec{\mathbb{P}}$ and $\vec{\mathbb{E}}$ are real-valued polarization and electric field, respectively. Here, the field and the polarization are assumed to be linearly polarized, and $|\cdot|$ calculates the vector length. If we recover its vector formulation and use its analytic signal [Eq. (9.8)], we obtain

$$\frac{\partial\vec{\mathcal{P}}_I}{\partial t} = \frac{e^2}{m_e}\int_{-\infty}^t \rho_e(t')\vec{\mathcal{E}}(t')\text{d}t' + \frac{\partial\rho_e}{\partial t}\frac{E_b}{\left|\vec{\mathcal{E}}(t)\right|^2/2}\vec{\mathcal{E}}(t) \tag{10.27}$$

Cornell University

By employing the property of Fourier transform, $\mathfrak{F}\left[\int_{-\infty}^{t} f(\tau)\,\mathrm{d}\tau\right] = \frac{1}{-i\omega}\mathfrak{F}\left[f(t)\right]$, with the recovered vector formulation, we obtain

$$\vec{\mathcal{P}}_I(t) = \frac{e^2}{m_e}\int_{-\infty}^{t}\int_{-\infty}^{t'}\rho_e(\tau)\vec{\mathcal{E}}(\tau)\,\mathrm{d}\tau\,\mathrm{d}t' + \int_{-\infty}^{t}\frac{\partial \rho_e}{\partial t'}\frac{E_b}{\left|\vec{\mathcal{E}}(t')\right|^2/2}\vec{\mathcal{E}}(t')\,\mathrm{d}t'$$

$$\Rightarrow \vec{\mathcal{P}}_I(\omega) = -\frac{e^2}{\omega^2 m_e}\mathfrak{F}\left[\rho_e(t)\vec{\mathcal{E}}(t)\right] + i\frac{2E_b}{\omega}\mathfrak{F}\left[\frac{\partial \rho_e}{\partial t}\frac{\vec{\mathcal{E}}(t)}{\left|\vec{\mathcal{E}}(t)\right|^2}\right]. \tag{10.28}$$

Eq. (10.28) is derived in the context of gas materials. In solids, due to relatively-short collision time between electrons, there is another contribution of "inverse Bremsstrahlung," leading to [29]

$$\vec{\mathcal{P}}_I(\omega) = -\frac{e^2}{\omega^2 m_e}\mathfrak{F}\left[\rho_e(t)\vec{\mathcal{E}}(t)\right] + i\frac{2E_b}{\omega}\mathfrak{F}\left[\frac{\partial \rho_e}{\partial t}\frac{\vec{\mathcal{E}}(t)}{\left|\vec{\mathcal{E}}(t)\right|^2}\right]. \tag{10.29}$$

By further employing the frequency-shifting property of Fourier transform, $\mathfrak{F}[e^{-i\omega_0 t}f(t)] = \mathfrak{F}[f(t)]\big|_{\omega-\omega_0}$, Eq. (10.28) can be represented with the "envelope" of analytic signals whose frequency component is under an offset frequency $\Omega = \omega - \omega_0$:

$$\vec{P}_I(\Omega) = -\frac{e^2}{\omega^2 m_e}\mathfrak{F}\left[\rho_e(t)\vec{E}(t)\right] + i\frac{2E_b}{\omega}\mathfrak{F}\left[\frac{\partial \rho_e}{\partial t}\frac{\vec{E}(t)}{\left|\vec{E}(t)\right|^2}\right]. \tag{10.30}$$

Similar to the unit transformation in deriving the 3D-UPPE, we apply $\left|\vec{\mathbb{A}}\right|^2 = \frac{\epsilon_0 n_{\mathrm{eff}}c}{2}\left|\vec{E}\right|^2$ to transform $\vec{E}$ with the unit of V/m into $\vec{\mathbb{A}}$ with the unit of $\sqrt{\mathrm{W/m^2}}$. We then obtain

$$\vec{P}'_I(\Omega) = \sqrt{\frac{\epsilon_0 n_{\mathrm{eff}}c}{2}}\vec{P}_I(\Omega) = -\frac{e^2}{\omega^2 m_e}\mathfrak{F}\left[\rho_e(t)\vec{\mathbb{A}}(t)\right] + i\frac{E_b\epsilon_0 n_{\mathrm{eff}}c}{\omega}\mathfrak{F}\left[\frac{\partial \rho_e}{\partial t}\frac{\vec{\mathbb{A}}(t)}{\left|\vec{\mathbb{A}}(t)\right|^2}\right], \tag{10.31}$$

which is used in Eq. (9.20).

As for the generated free-electron density ρ_e, it satisfies

$$\partial_t \rho_e = W\left(N_g - \rho_e\right) + \frac{\sigma_{IB}}{E_b}\rho_e\left|\vec{\mathbb{E}}\right|^2 - \frac{\rho_e}{\tau_r}$$

$$\approx W\left(N_g - \rho_e\right) \tag{10.32}$$

with $W(t)$ being the ionization rate, which is calculated with previously derived $W_{\mathrm{AC}}^{\mathrm{PPT}}$ [Eq. (10.24)]. N_g is the total neutral-gas density. σ_{IB} is the cross section of inverse Bremsstrahlung:

$$\sigma_{\mathrm{IB}} = \frac{e^2}{n\omega c\epsilon_0 m_e}\frac{\omega\tau_c}{1+\omega^2\tau_c^2}. \tag{10.33}$$

Cornell University

In gases, the collision time τ_c is so large that σ_{IB} is close to zero. In addition, its recombination time seems to be a few nanoseconds to microseconds (author comment: I'm not super sure), which is long compared to the typical pulse duration investigated, so it can be ignored. In the perturbative regime,

$$\rho_e(t) \approx N_g \int_{-\infty}^{t} W(\tau)\,\mathrm{d}\tau \quad , \rho_e(t \to -\infty) = 0. \tag{10.34}$$

Determining which ω to use for a pulse can be confusing and create difficulties in deriving the Keldysh parameter that is required for photoionization computations. As a result, rather than using a single-scalar Keldysh parameter, we compute the instantaneous frequency at each temporal position with $\omega(t) = \omega_0 - \frac{\mathrm{d}\phi}{\mathrm{d}t}$ (ϕ being the phase of $\vec{\mathbb{A}}(t)$ and ω_0 being the free parameter of UPPE) and apply

$$\gamma(t) = \sqrt{\frac{E_b}{2U_p(t)}} \quad , U_p(t) = \frac{e^2\left|\vec{\mathbb{A}}(t)\right|^2}{2m_e\left[\omega(t)\right]^2 \epsilon_0 n_{\mathrm{eff}}c}. \tag{10.35}$$

Furthermore, we replace $\left|\vec{\mathbb{E}}\right|$ with $\left|\vec{\mathbb{A}}\right|$ in $W_{\mathrm{AC}}^{\mathrm{PPT}}$ [Eq. (10.24)] and finally get

$$W_{\mathrm{AC}}^{\mathrm{PPT}}(t) = \sum_m \left|C_{n^*,\ell^*}\right|^2 f(\ell,m)\frac{E_b}{\hbar}\sqrt{\frac{6}{\pi}}\left(\sqrt{\frac{\epsilon_0 n_{\mathrm{eff}}c}{2}}\frac{\kappa}{\left|\vec{\mathbb{A}}(t)\right|\sqrt{1+\gamma(t)^2}}\right)^{2n^*-|m|-3/2}$$
$$\times A_m(\gamma(t))\mathrm{e}^{-\sqrt{\frac{\epsilon_0 n_{\mathrm{eff}}c}{2}}\frac{\kappa}{3\left|\vec{\mathbb{A}}(t)\right|}g(\gamma(t))}. \tag{10.36}$$

10.4 Ionization and UPPE for solids

It is worth noting that the derivation we have discussed belongs to gases. A few modifications need to be considered.

First, due to the valence and conduction bands, the ionized electrons do not become free electrons. Thus, the ionization rate equation is different [29]:

$$W(t) = \frac{1}{N_e}\frac{2\omega}{9\pi}\left(\frac{\omega m_e}{\hbar\sqrt{\Gamma}}\right)^{3/2} Q(\gamma',x)\mathrm{e}^{-\alpha\lceil x\rceil}, \tag{10.37}$$

where

$$\gamma' = \frac{\gamma}{\sqrt{2}} \tag{10.38a}$$

$$\Gamma = \frac{(\gamma')^2}{1+(\gamma')^2}, \qquad \Xi = \frac{1}{1+(\gamma')^2} \tag{10.38b}$$

$$Q(\gamma',x) = \sqrt{\frac{\pi}{2K(\Xi)}}\sum_{S=0}^{\infty}\mathrm{e}^{-S\alpha'}B_0(\sqrt{\beta'(S+2\nu')}) \tag{10.38c}$$

$$\alpha' = \pi\frac{K(\Gamma)-E(\Gamma)}{E(\Xi)}, \qquad \beta' = \frac{\pi^2}{4K(\Xi)E(\Xi)} \tag{10.38d}$$

$$x = \frac{2}{\pi} \frac{E_b}{\hbar\omega} \frac{E(\Xi)}{\sqrt{\Gamma}} \tag{10.38e}$$

$$\nu' = \lceil x \rceil - x \tag{10.38f}$$

The definition of γ' here differs from the Keldysh parameter by a factor of $1/\sqrt{2}$. ν' bears the similarity with $(\tilde{n} - \nu)_0$ in Eq. (10.13). β' is normalized such that it is one when $\gamma' \gg 1$ (or $\gamma \gg 1$) in the multiphoton-ionization regime.
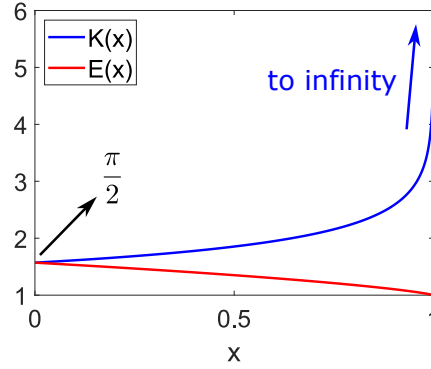

Figure 10.3: Complete elliptic integral of the first K and second E kinds.

In addition to a different ionization rate for solids, due to relatively-short collision time between electrons, there is another contribution of "inverse Bremsstrahlung." Eq. (10.31) is revised into

$$\vec{P}'_I(\Omega) = -\frac{e^2}{\omega^2 m_e} \frac{(-i + \omega\tau_c)\,\omega\tau_c}{1 + \omega^2\tau_c^2} \mathfrak{F}\left[\rho_e(t)\vec{\mathbb{A}}(t)\right] + i\frac{E_b\epsilon_0 n_{\mathrm{eff}}c}{\omega} \mathfrak{F}\left[\frac{\partial\rho_e}{\partial t} \frac{\vec{\mathbb{A}}(t)}{\left|\vec{\mathbb{A}}(t)\right|^2}\right]. \tag{10.39}$$

In silica, the average collision time of electrons is $1\,\mathrm{fs}$.

All terms in Eq. (10.32) regarding the generated free-electron density need to be retained:

$$\partial_t \rho_e = W\left(N_g - \rho_e\right) + \frac{\sigma_{IB}}{E_b}\rho_e\left|\vec{\mathbb{E}}\right|^2 - \frac{\rho_e}{\tau_r}$$

$$= \left(-W + \frac{\sigma_{\mathrm{IB}}}{E_b}\left|\vec{\mathbb{E}}\right|^2 - \frac{1}{\tau_r}\right)\rho_e + WN_g \tag{10.40}$$

In solids, N_g is the density of neutral atoms (silica's N_g is $2.20 \times 10^{28}\,\mathrm{m}^{-3}$).

10.5 Required steps in implementations

Although we have derived A_0 in its simplest form [Eq. (10.12)], the computation of an imaginary error function, $\mathrm{erfi}(x)$, in it is relatively slow. However, there is an easy solution. Notice that $\beta(\gamma)$ spans only from 0 to 2 while $(\tilde{n} - \nu)_S$ from 0 to $S + 1$. Therefore, the range of the input argument of $\mathrm{erfi}(x)$ is limited, from 0 to $\sqrt{2(S+1)} = \sqrt{22}$ if we pick $S = 10$. We find simulations much faster by creating a lookup table for $\mathrm{erfi}(x)$ beforehand and applying linear interpolation to the values during simulations.

Cornell University

In computing $\vec{\mathbb{A}}(t)/\left|\vec{\mathbb{A}}(t)\right|^2$, it is spurious to apply division to places without a field, which might produce a mysterious result. To avoid this problem, we reset and restrict the maximum of this inverse power to $1/\left(\max_t \left|\vec{\mathbb{A}}(t)\right|^2/10^5\right)$ so that it does not create a weird result at no fields. This operation will not result in a wrong outcome since it correctly ensures that $\vec{\mathbb{A}}(t)/\left|\vec{\mathbb{A}}(t)\right|^2 \approx 0$ at zero fields. We have also considered making the denominator $\left|\vec{\mathbb{A}}(t)\right|^2$ a constant $\max_t \left|\vec{\mathbb{A}}(t)\right|^2$ for each propagation z, proposed by Saleh *et al.* [23]. However, in simulations with multiple pulses, picking the maximum peak power from the strongest pulse underestimates the ionization of other weaker pulses. We, therefore, abandoned Saleh's approach and resorted to ours. Additionally, to avoid any spurious result from the numerical precision error, we apply $W_{\mathrm{AC}}^{\mathrm{PPT}}(\left|\vec{\mathbb{A}}\right| < \max_t \left|\vec{\mathbb{A}}(t)\right|/10^2) = 0$ after computing $W_{\mathrm{AC}}^{\mathrm{PPT}}$ from Eq. (10.36). This ensures that the ionization rate is zero when there is no field, because there are divisions to $\left|A(t)\right|$ in $W_{\mathrm{AC}}^{\mathrm{PPT}}$ as well. We find this step important; otherwise, the ionization rate can grow right before the pulse when the field is too weak due to the numerical precision error.

10.6   Confluent hypergeometric function

In addition to the imaginary error function, there is another special function that can be used to represent B_m, for all m, more easily. This is the "confluent hypergeometric function" $\Phi(a, c, z)$:

$$\Phi(a, c, z) \equiv {}_1F_1(a; c; z) = \sum_{k=0}^{\infty} \frac{(a)_k z^k}{(c)_k k!}, \tag{10.41}$$

where $(a)_k = \frac{\Gamma(a+k)}{\Gamma(a)}$. It has an integral representation:

$$\Phi(a, c, z) = \frac{\Gamma(c)}{\Gamma(a)\Gamma(c-a)} \int_0^1 e^{zt} t^{a-1} (1-t)^{c-a-1}\, dt \quad , \mathrm{Re}[c] > \mathrm{Re}[a] > 0. \tag{10.42}$$

With it, we can write B_m as

$$\begin{aligned}
B_m(x) &= \frac{x^{2|m|+1}}{2} \frac{\Gamma(|m|+1)\sqrt{\pi}}{\Gamma(|m|+\frac{3}{2})} \Phi(|m|+1, |m|+\frac{3}{2}, -x^2) \\
&= \frac{x^{2|m|+1}}{2} \frac{\Gamma(|m|+1)\sqrt{\pi}}{\Gamma(|m|+\frac{3}{2})} e^{-x^2} \Phi(\frac{1}{2}, |m|+\frac{3}{2}, x^2),
\end{aligned} \tag{10.43}$$

where we apply Kummer's transformation, $\Phi(a, c, z) = e^z \Phi(c-a, c, -z)$. We can see that with the relation

$$\mathrm{erfi}(x) = \frac{2x}{\sqrt{\pi}} \Phi(\frac{1}{2}, \frac{3}{2}, x^2) = \frac{2x}{\sqrt{\pi}} e^{x^2} \Phi(1, \frac{3}{2}, -x^2), \tag{10.44}$$

Eq. (10.43) can clearly be reduced to Eq. (10.11) when $m = 0$.

Cornell University

Bibliography

[1] A. M. Heidt, "Efficient Adaptive Step Size Method for the Simulation of Supercontinuum Generation in Optical Fibers", J. Light. Technol. **27**, 3984–3991 (2009).

[2] S. Balac and F. Mahé, "Embedded Runge-Kutta scheme for step-size control in the interaction picture method", Comput. Phys. Commun. **184**, 1211–1219 (2013).

[3] B. C. Hall, "The baker—campbell—hausdorff formula", in *Lie groups, lie algebras, and representations: an elementary introduction* (Springer New York, New York, NY, 2003), pp. 63–90.

[4] R. H. Stolen, J. P. Gordon, W. J. Tomlinson, and H. A. Haus, "Raman response function of silica-core fibers", J. Opt. Soc. Am. B **6**, 1159–1166 (1989).

[5] Q. Lin and G. P. Agrawal, "Raman response function for silica fibers", Opt. Lett. **31**, 3086–3088 (2006).

[6] Y.-H. Chen and F. Wise, "Unified and vector theory of Raman scattering in gas-filled hollow-core fiber across temporal regimes", APL Photonics **9**, 030902 (2024).

[7] Y.-H. Chen, "Tutorial of Fourier and Hankel transforms for ultrafast optics", arXiv preprint arXiv: 2412.20698 (2025).

[8] V. Magni, G. Cerullo, and S. D. Silvestri, "High-accuracy fast Hankel transform for optical beam propagation", J. Opt. Soc. Am. A **9**, 2031–2033 (1992).

[9] A. E. Siegman, "Quasi fast Hankel transform", Opt. Lett. **1**, 13–15 (1977).

[10] G. P. Agrawal and M. Lax, "End correction in the quasi-fast Hankel transform for optical-propagation problems", Opt. Lett. **6**, 171–173 (1981).

[11] W. Wang, Y. Eisenberg, Y.-H. Chen, C. Xu, and F. Wise, "Efficient temporal compression of 10-μJ pulses in periodic layered Kerr media", Opt. Lett. **49**, 5787–5790 (2024).

[12] F. Poletti and P. Horak, "Description of ultrashort pulse propagation in multimode optical fibers", J. Opt. Soc. Am. B **25**, 1645–1654 (2008).

[13] B. Kibler, J. M. Dudley, and S. Coen, "Supercontinuum generation and nonlinear pulse propagation in photonic crystal fiber: influence of the frequency-dependent effective mode area", Appl. Phys. B **81**, 337–342 (2005).

[14] J. Lægsgaard, "Mode profile dispersion in the generalized nonlinear schrödinger equation", Opt. Express **15**, 16110–16123 (2007).

[15] Y.-H. Chen, P. Sidorenko, E. Antonio-Lopez, R. Amezcua-Correa, and F. Wise, "Efficient soliton self-frequency shift in hydrogen-filled hollow-core fiber", Opt. Lett. **47**, 285–288 (2022).

[16] M. F. Saleh, W. Chang, P. Hölzer, A. Nazarkin, J. C. Travers, N. Y. Joly, P. St. J. Russell, and F. Biancalana, "Theory of Photoionization-Induced Blueshift of Ultrashort Solitons in Gas-Filled Hollow-Core Photonic Crystal Fibers", Phys. Rev. Lett. **107**, 203902 (2011).

[17] Z. Y. Huang, Y. F. Chen, F. Yu, D. Wang, R. R. Zhao, Y. Zhao, S. F. Gao, Y. Y. Wang, P. Wang, M. Pang, and Y. X. Leng, "Continuously wavelength-tunable blueshifting soliton generated in gas-filled photonic crystal fibers", Opt. Lett. **44**, 1805–1808 (2019).

[18] J. C. Travers, W. Chang, J. Nold, N. Y. Joly, and P. St. J. Russell, "Ultrafast nonlinear optics in gas-filled hollow-core photonic crystal fibers [Invited]", J. Opt. Soc. Am. B **28**, A11–A26 (2011).

[19] Z. Huang, D. Wang, Y. Chen, R. Zhao, Y. Zhao, S. Nam, C. Lim, Y. Peng, J. Du, and Y. Leng, "Wavelength-tunable few-cycle pulses in visible region generated through soliton-plasma interactions", Opt. Express **26**, 34977–34993 (2018).

[20] P. A. Carpeggiani, G. Coccia, G. Fan, E. Kaksis, A. Pugžlys, A. Baltuška, R. Piccoli, Y.-G. Jeong, A. Rovere, R. Morandotti, L. Razzari, B. E. Schmidt, A. A. Voronin, and A. M. Zheltikov, "Extreme Raman red shift: ultrafast multimode nonlinear space-time dynamics, pulse compression, and broadly tunable frequency conversion", Optica **7**, 1349–1354 (2020).

[21] M. Geissler, G. Tempea, A. Scrinzi, M. Schnürer, F. Krausz, and T. Brabec, "Light Propagation in Field-Ionizing Media: Extreme Nonlinear Optics", Phys. Rev. Lett. **83**, 2930–2933 (1999).

[22] W. Chang, A. Nazarkin, J. C. Travers, J. Nold, P. Hölzer, N. Y. Joly, and P. St. J. Russell, "Influence of ionization on ultrafast gas-based nonlinear fiber optics", Opt. Express **19**, 21018–21027 (2011).

[23] M. F. Saleh and F. Biancalana, "Ultra-broadband supercontinuum generation in gas-filled photonic-crystal fibers: the epsilon-near-zero regime", Opt. Lett. **46**, 1959–1962 (2021).

[24] J. O. Smith, *Mathematics of the Discrete Fourier Transform (DFT)* (W3K Publishing, 2007).

[25] M. Conforti, A. Marini, D. Faccio, and F. Biancalana, "Negative frequencies get real: a missing puzzle piece in nonlinear optics", arXiv preprint arXiv:1305.5264, `10.48550/ARXIV.1305.5264` (2013).

[26] A. M. Perelomov, V. S. Popov, and M. V. Terent'ev, "Ionization of Atoms in an Alternating Electric Field", Sov. Phys. JETP **23**, 924 (1966).

[27] A. Hussien, "Ionization of diatomic molecules in intense laser fields", PhD thesis (Humboldt-Universität zu Berlin, Oct. 2015).

[28] A. Einstein, "Über einen die Erzeugung und Verwandlung des Lichtes betreffenden heuristischen Gesichtspunkt", Ann. Phys. **322**, 132–148 (1905).

[29] A. Couairon, L. Sudrie, M. Franco, B. Prade, and A. Mysyrowicz, "Filamentation and damage in fused silica induced by tightly focused femtosecond laser pulses", Phys. Rev. B **71**, 125435 (2005).

[30] F. A. Ilkov, J. E. Decker, and S. L. Chin, "Ionization of atoms in the tunnelling regime with experimental evidence using Hg atoms", J. Phys. B: At. Mol. Opt. Phys. **25**, 4005–4020 (1992).

Cornell University